

VSP analysis for azimuthal anisotropy: AVAZ, VVAZ and S-wave splitting in Altamont-Bluebell field

Khaled Al Dulaijan, Gary F. Margrave, and Joe Wong.

ABSTRACT

Within the Altamont-Bluebell survey, multiple VSP datasets were acquired. The first dataset was a conventional zero-offset VSP. The second dataset was six shots of offset VSPs. The objective of those shots was to estimate VTI Thomsen parameters to aid with 3D processing of seismic data, and also to create a HTI model for fracture characterization of the reservoirs. However, these offset VSPs were limited in terms of depth, offset, and azimuthal coverage, and walkaway VSPs would have been a better choice for such an objective, but certainly more expensive. The third dataset was a 4-component VSP. Its objective is S-wave splitting analysis for fracture characterization of the reservoirs.

In this paper, we began with the raw field data, applied processing, including some twists in order to use surface seismic methods of AVAZ and VVAZ on VSP data, which resulted in final products of azimuthal anisotropy intensity and orientation parameters. Offset VSPs were processed through the VSP-CDP transform, then AVAZ analysis was applied. A VVAZ workflow is developed here for offset, walkaround, or walkaway VSPs using a method for surface seismic, and interval anisotropy properties are calculated for each receiver. For AVAZ and VVAZ, deeper levels including the deeper target of Wasatch-180 are more reliable because of better coverage. S-wave analysis is carried out using Alford (1986) 4-C rotation to separate fast and slow modes. This method assumes that the symmetry axis is vertically invariant. To overcome this assumption, a layer stripping technique was applied using Winterstien and Meadows (1991).

VSP DATA ACQUISITION

A zero-offset VSP (ZVSP) and 6 offset VSPs were acquired using a P-wave source on surface and a 2-level tool of 3-C geophones in the borehole. Another 4-C VSP was acquired using an S-wave source and 3-C geophones with attached gyro to obtain tool orientation. Notice that although the number of components that are recorded is 6, it is called 4-C VSP because only the four horizontal components are used and provide additional information to zero-offset VSP. The natural frequency of the geophones is 15 Hz, and the vibroseis sweep is 4-96 Hz. The total depth (TD) is 14240' referenced to Kelly Bushing (KB). The surface elevation of the borehole is 5254' above mean sea level (MSL), while the Kelly Bushing elevation is 5288' above MSL. Table 1 summarizes the geometry of all VSP datasets.

The two zero-offset VSPs were used to create a velocity model that has been used in different processing steps for the other VSPs. For AVAZ and VVAZ, shots 2 to 8 were used. The locations of the sources are shown in Figure 1. Figure 2 shows the acquired depths, offset, and azimuths for each shot. Depths from 8700' to 14000' are covered by 6 shots, and depths above 3400' were covered by 4 shots. For all depths, one of the shots was

a zero-offset VSP. The data quality was decent without noticeable casing or cementing effects.

Shot number	Shot-Borehole offset (ft)	Shot Azimuth (°)	Top receiver depth from KB (ft)	Bottom receiver depth from KB (ft)
1 (ZVSP)	408	156	480	3580
2 (ZVSP)	360	360	3400	14050
3	5755	170	8700	14050
4	3184	170	3300	8650
5	6332	108	3400	14050
6	2542	102	3300	14050
7	14954	95	8550	14000
8	10889	88	8550	14000
9	672	344	3300	14050
10	672	344	3300	14050

Table 1 Shot and receiver geometry.

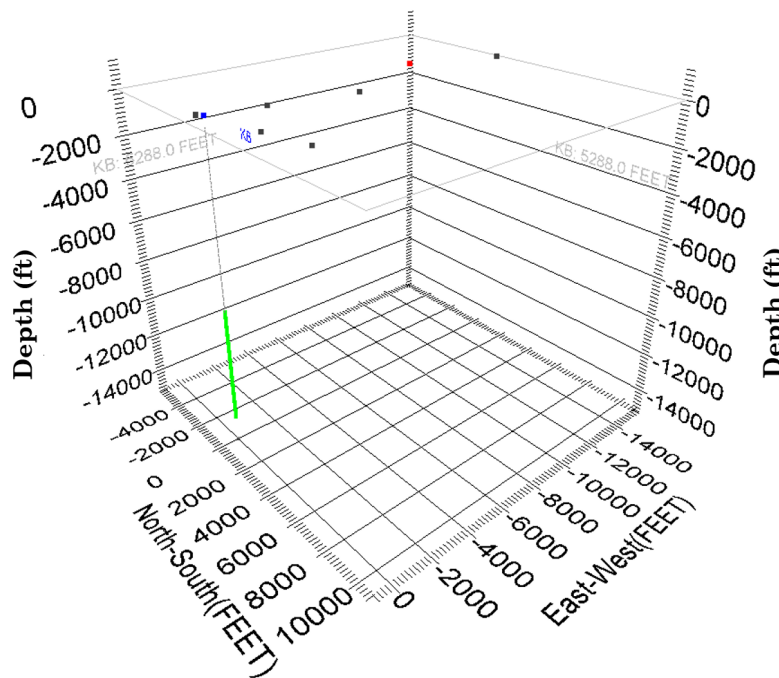


Figure 1 The geometry of the VSP survey. Shots are on surface indicated by small boxes. Live receivers for the red shot are in the borehole indicated by green dots.

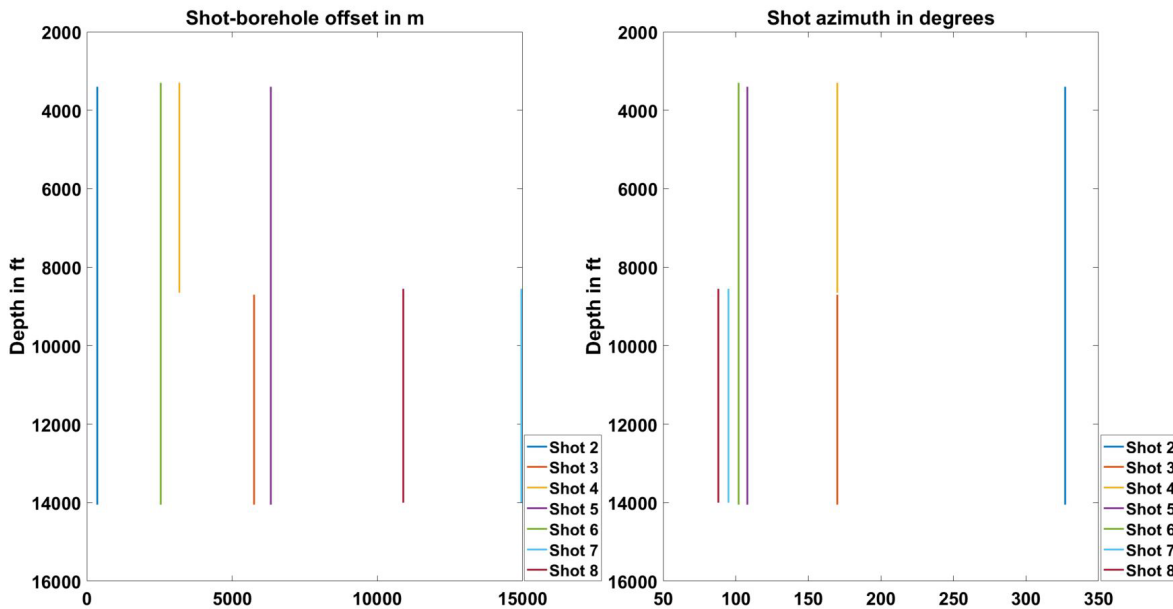


Figure 2 Acquired depths, offset, and azimuths for each shot.

The last dataset was a 4-component VSP and was acquired during two runs. Since there were no vertical shots, we have used shots from offset VSP to re-orient the tool into East-West and North-South directions as explained in the S-wave splitting section.

VSP DATA PROCESSING

We processed the zero-offset VSP, offset VSPs and 4-C VSP for different purposes and therefore used different workflows. We began the processing with SEG Y files. For zero-offset VSP, processing was straight-forward, with major processing steps being: geometry assignment, stacking, bandpass filtering, picking of P-wave first breaks, P and S wavefield separation, and deconvolution. Stacking here is different than surface seismic data processing. Basically in the field, each shot is repeated 3 to 5 times to reduce random noise. Noisy traces are deleted, and the rest of traces were stacked to form a single trace between shot and receiver. Bandpass filtering was applied to attenuate noise below 4 Hz and above 120 Hz. The first breaks are picked on the trough of the first arrival waveform, and those picks are used to create the P-wave velocity model used later for offset VSPs wavefield separation and for sonic log calibration. P-wave first breaks were used to calculate an amplitude decay function. Then, exponential gain was applied to account for amplitude decay as a function of time with f factor ($f=2.0$) as follows:

$$A(t) = A_0(t)t^f \quad (1)$$

For wavefield separation, time shifts and median filters were utilized. First, the downgoing P wave was aligned using P-wave first breaks. Then, a median filter was applied to remove the downgoing P wave from the vertical-component data. The filtered downgoing P wave is used for VSP deconvolution.

One of the advantages of VSP geometry over surface seismic geometry is that the source signature is known and can be used for deterministic deconvolution. After wavefield separation, a window is chosen around the first breaks on the downgoing P wave. The waveform inside that window can approximate the source signature. Figure 3 shows vertical-component data after P-wave first break picking with AGC applied for display. Figure 4 and Figure 5 show the separated upgoing P-wave field after amplitude recovery and its amplitude spectrum respectively. This offset VSP shot and its amplitude spectrum after deconvolution are shown in Figure 6 and Figure 7 respectively.

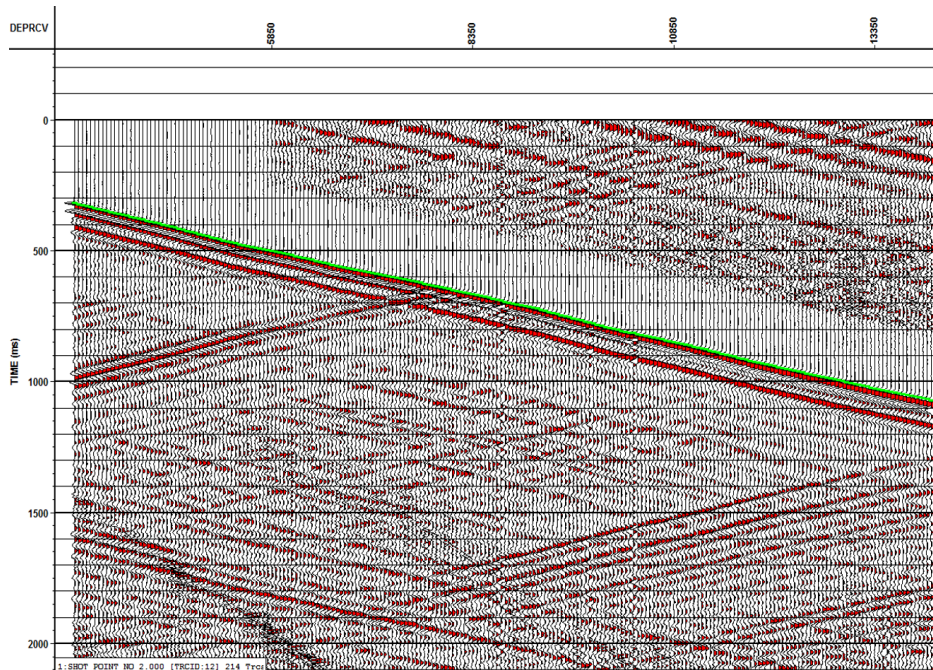


Figure 3 Vertical-component of a zero-offset VSP common-shot gather, with P-wave first arrival times indicated by green picks. AGC is applied for display.

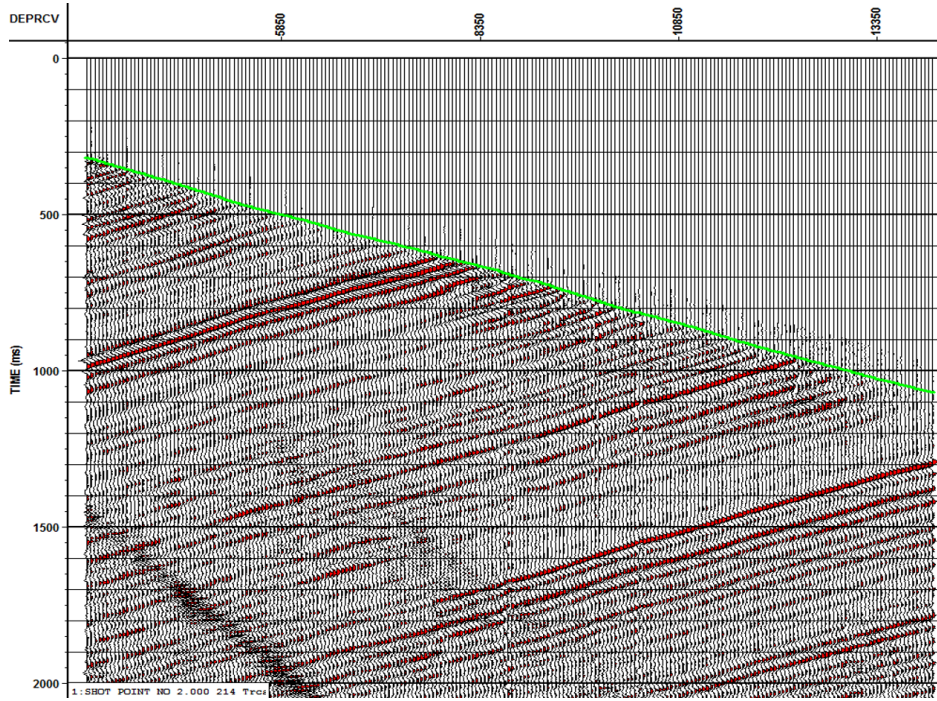


Figure 4 Upgoing P-wave of a zero-offset VSP common-shot gather after wavefield separation. P-wave arrival times indicated by green picks.

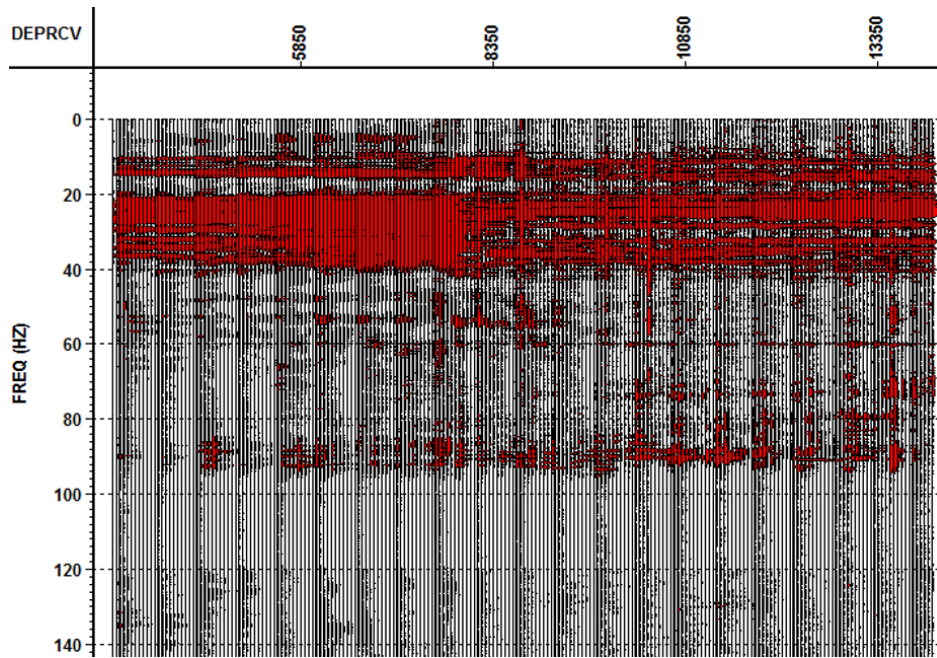


Figure 5 Amplitude spectra of the zero-offset VSP prior to deconvolution, displayed in Figure 4

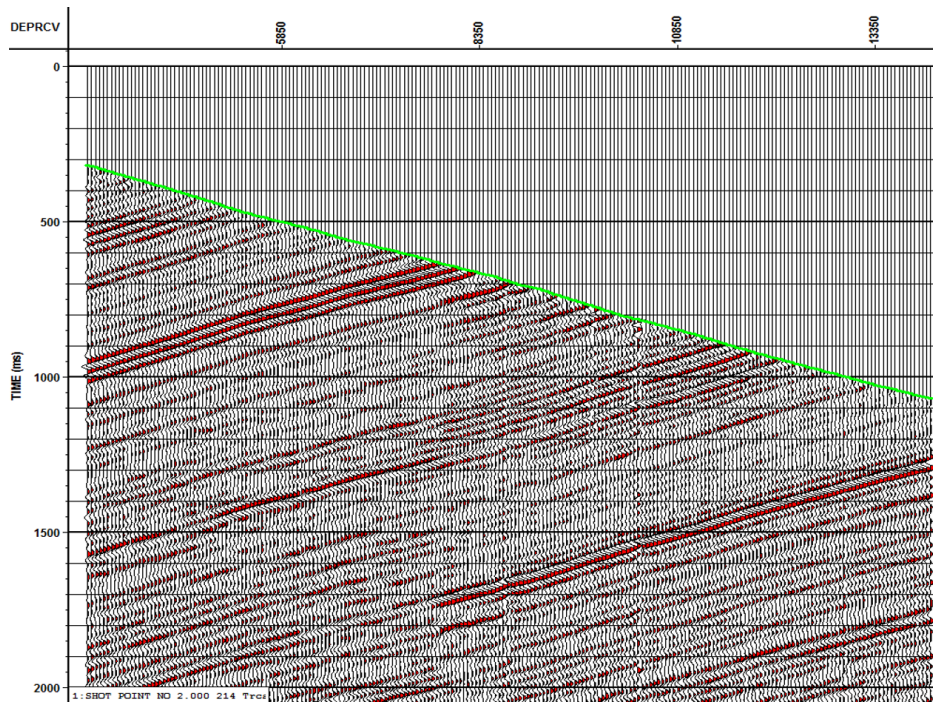


Figure 6 Upgoing P-wave of a zero-offset VSP common-shot gather after deterministic deconvolution. P-wave arrival times indicated by green picks.

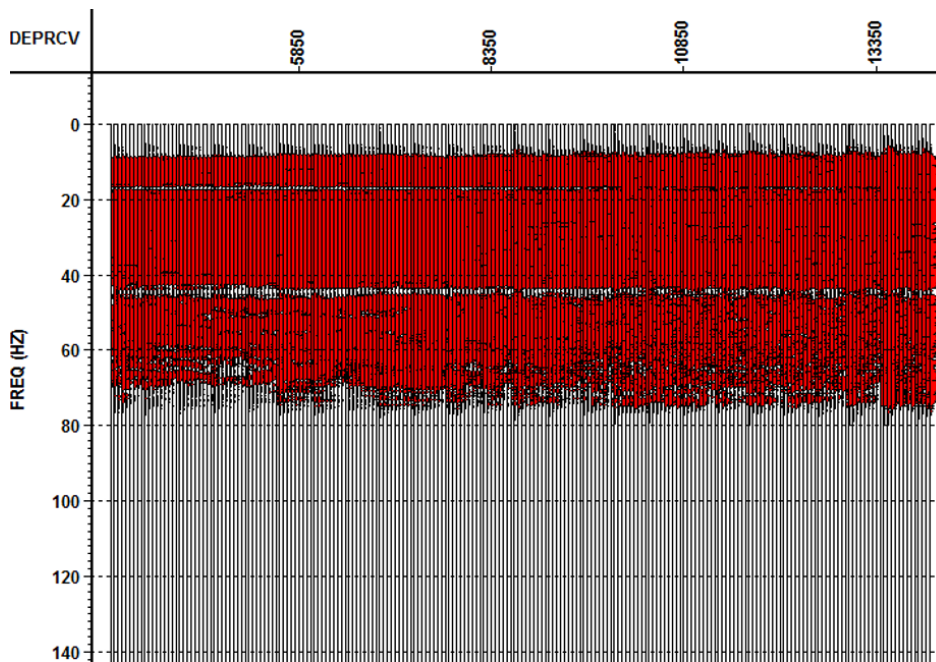


Figure 7 Amplitude spectra of the zero-offset VSP after deconvolution, displayed in Figure 6

Compared to zero-offset VSP processing, offset VSPs are harder to process. The main difficulty is due to the fact that P-wave and S-wave modes are all captured by the three components, and therefore require an extra effort in separating different modes of body waves. A model-based wavefield separation processing workflow for offset VSPs was implemented and is summarized in Figure 8.

The first rotation applied to the 3-components is horizontal rotation to rotate the two horizontal components into a component within the propagation plane and a component transverse to the propagation plane, as explained by Figure 9. After horizontal rotation, the radial component will capture most of the data between the two rotated horizontal components, while the data is minimized for the transverse component. The other rotation is vertical rotation. After vertical orientation, the direct component is oriented towards the source and has most of the downgoing P-wave energy, as explained by Figure 10. The vertical (Z) and two horizontal (Y and X) components are shown respectively by Figure 11, Figure 12, and Figure 13 after applying bandpass filter, P-wave first breaks picking, and amplitude recovery. After horizontal rotation, the energy was maximized on the radial component as can be seen in Figure 14, and minimized on the transverse component as can be seen in Figure 15.

Vertical rotation is not the ideal way to separate upgoing P-wave and S-wave fields because the required rotation is temporally variant. However, it is applied to remove downgoing strong P-wave energy before time-variant rotation. After the vertical rotation, the direct component in Figure 16 is oriented toward the source, as can be seen by the maximized energy of P-wave first arrival times. The upgoing P-wave and S-wave fields are distributed between this component and the perpendicular component (the component orthogonal to the direct component) in Figure 17. Median and FK filters were used then to remove the downgoing P wavefield from direct and perpendicular components shown in Figure 18 and Figure 19 where the data are mostly upgoing P-wave and S-wave energy. Inverse vertical rotation is applied then to rotate the data back to vertical (Z') and radial (X') and shown respectively in Figure 20 and Figure 21.

Next, a time-variant rotation is applied to separate upgoing P-wave energy shown in Figure 22 and upgoing S-wave energy shown Figure 23. Deconvolution and NMO correction are applied to the upgoing P wave. After NMO correction, events are supposed to match two-way-time of surface seismic events. Figure 24 shows the VSP-CDP transform (left) and upgoing P-wave data (right) after deconvolution and NMO. Figure 13

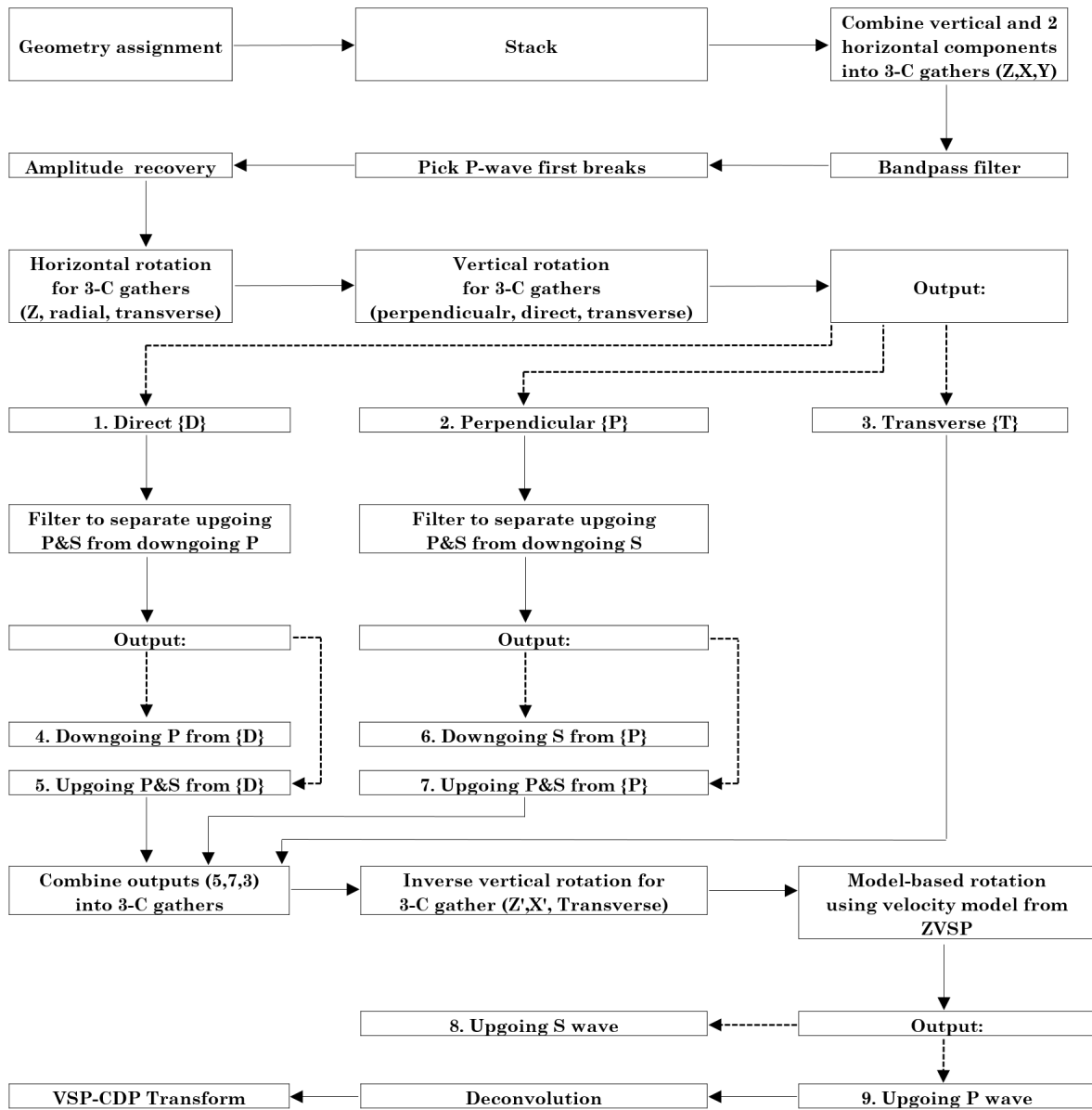


Figure 8 Model-based wavefield separation processing workflow for offset VSPs.

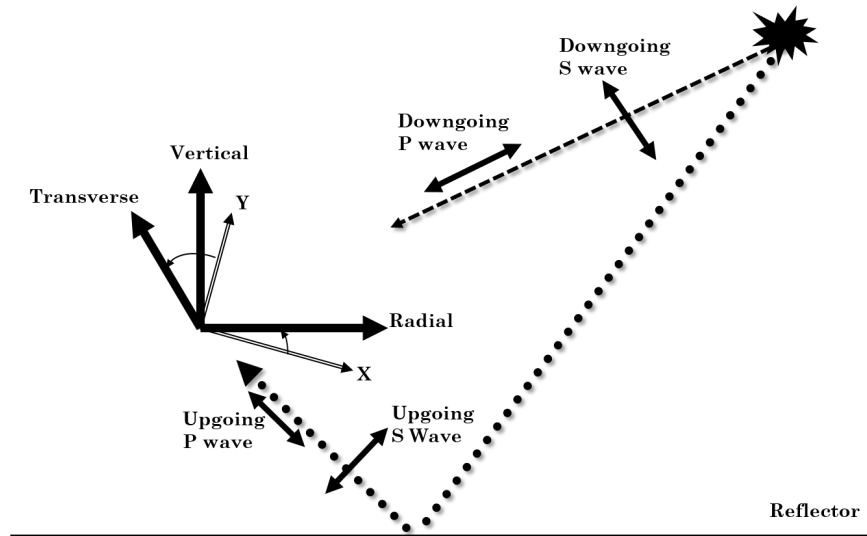


Figure 9 Horizontal rotation with different P and S wavefields illustrated by dashed line for downgoing raypath and dotted line for upgoing raypath. Original acquisition is along arbitrary X and Y orthogonal axes. After horizontal orientation, radial component is oriented at the propagation plane and contains most of the energy between horizontal components.

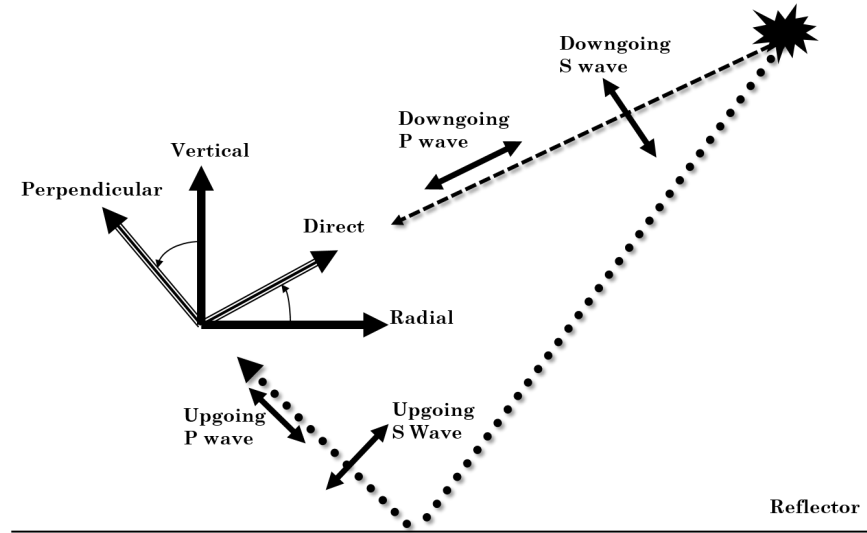


Figure 10 Vertical rotation with different P and S wavefields illustrated by dashed line for downgoing raypath and dotted line for upgoing raypath. After vertical orientation, direct component is oriented towards the source and contains most of the downgoing P-wave energy.

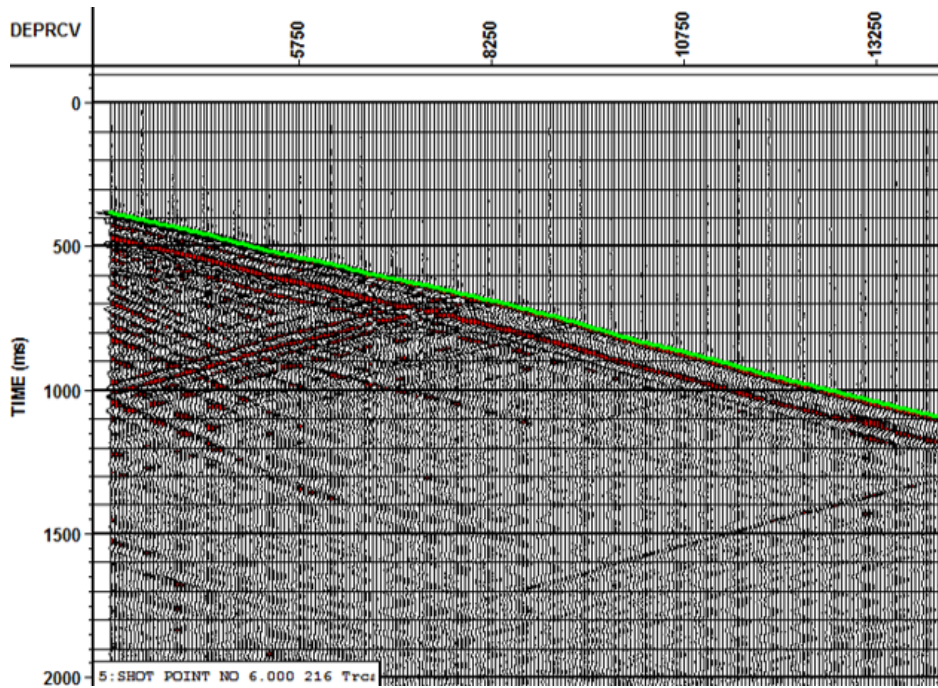


Figure 11 Vertical-component (Z) of an offset VSP common-shot gather after amplitude recovery and picking of P-wave first arrival times, indicated by green picks.

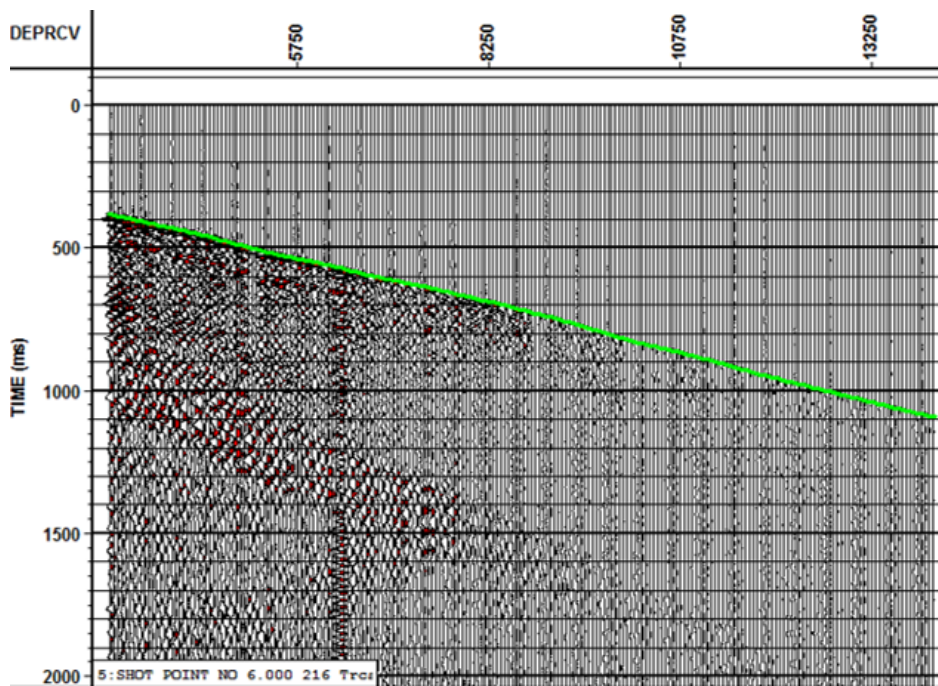


Figure 12 Horizontal-component (X) of an offset VSP common-shot gather after amplitude recovery and picking of P-wave first arrival times, indicated by green picks.

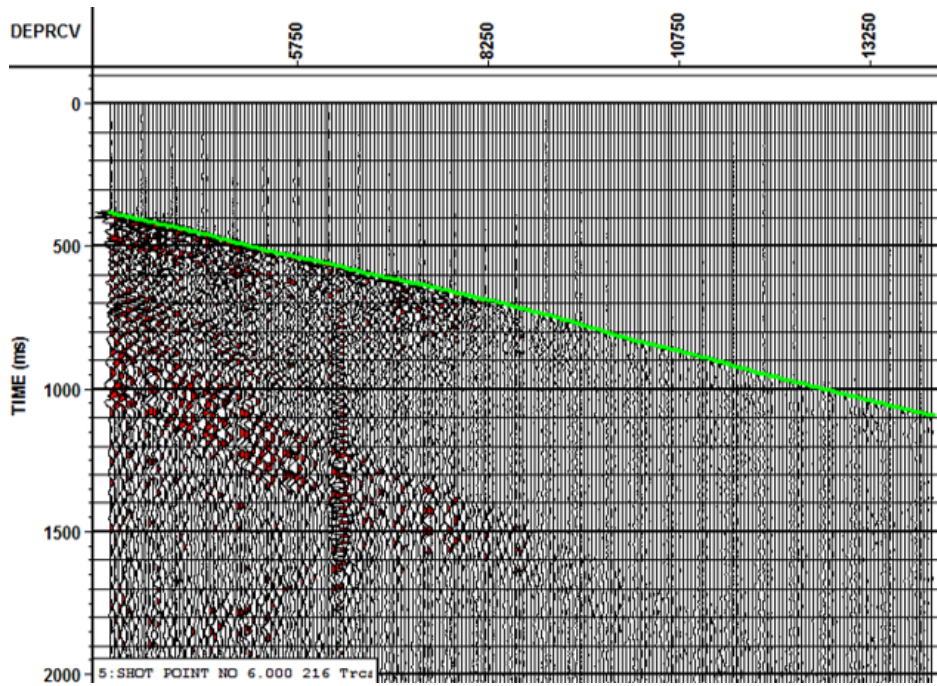


Figure 13 Horizontal-component (Y) of an offset VSP common-shot gather after amplitude recovery and picking of P-wave first arrival times, indicated by green picks.

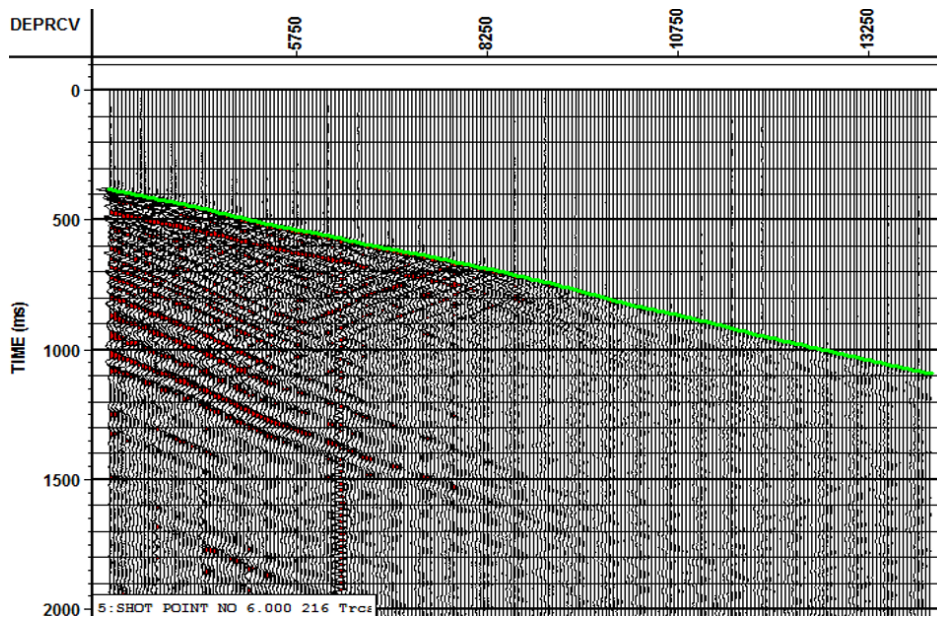


Figure 14 Radial-component (R) of an offset VSP common-shot gather after horizontal rotation.

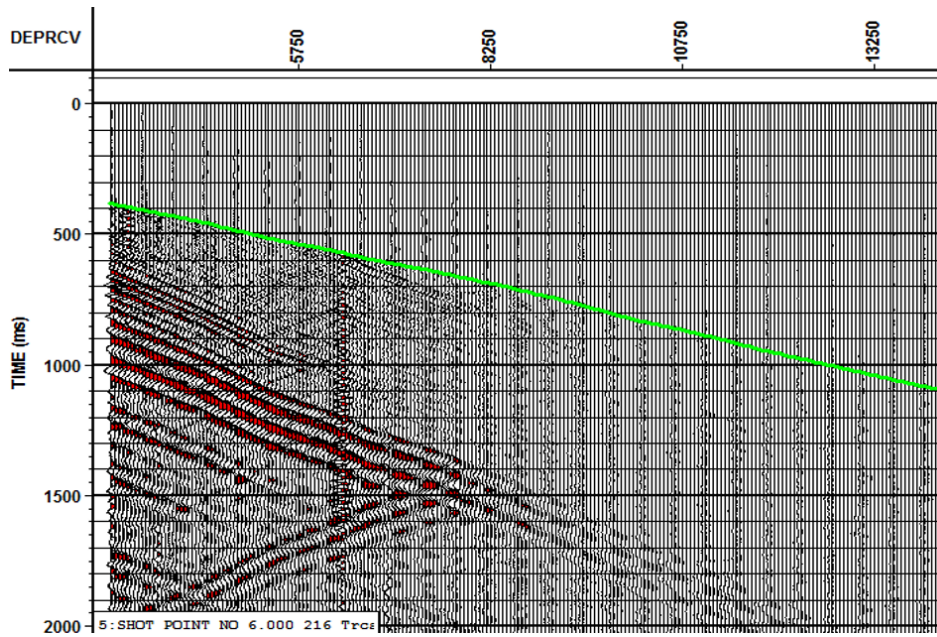


Figure 15 Transverse-component (T) of an offset VSP common-shot gather after horizontal rotation.

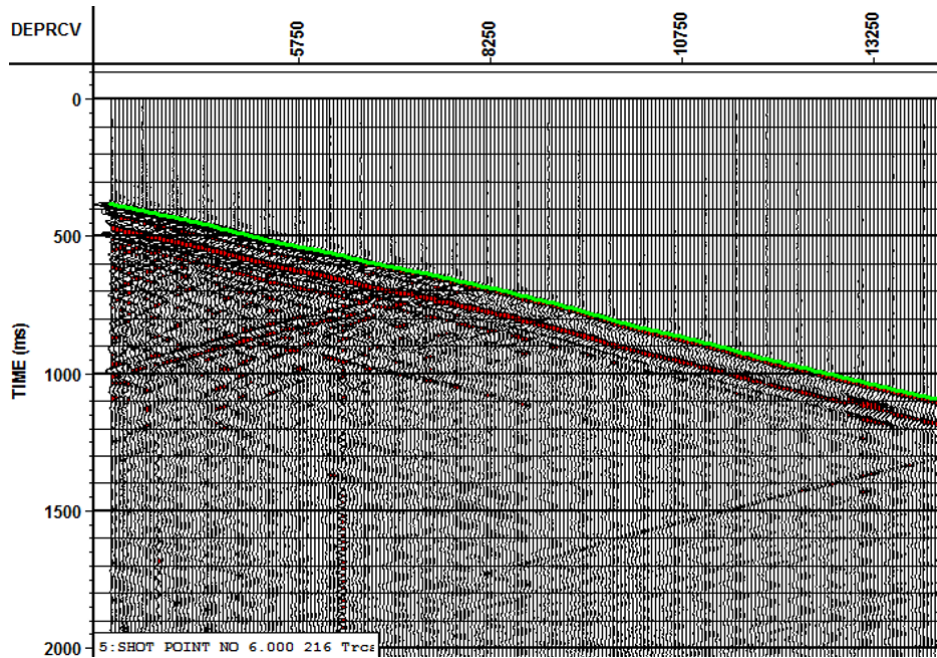


Figure 16 Direct-component (D) of an offset VSP common-shot gather after vertical rotation.

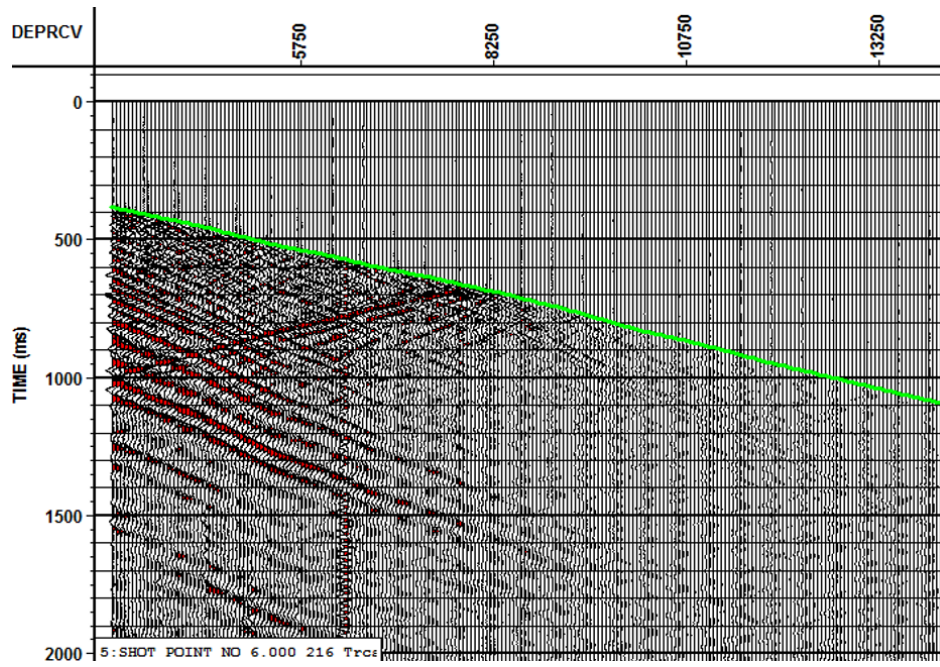


Figure 17 Perpendicular-component (P) of an offset VSP common-shot gather after vertical rotation.

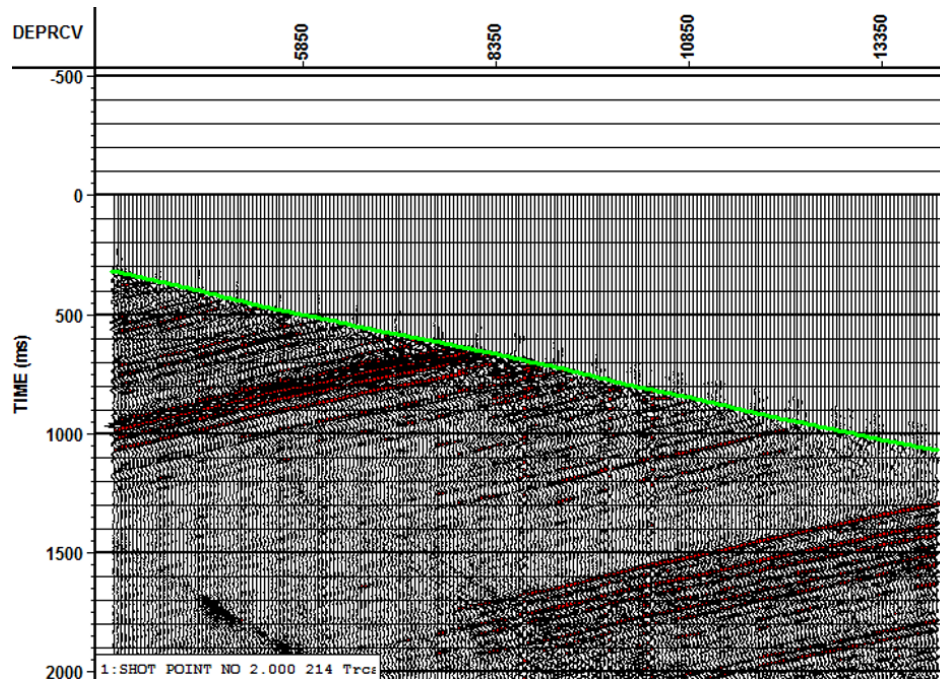


Figure 18 Upgoing P & S wavefields on direct-component (D) of an offset VSP common-shot gather after filtering out downgoing wavefields.

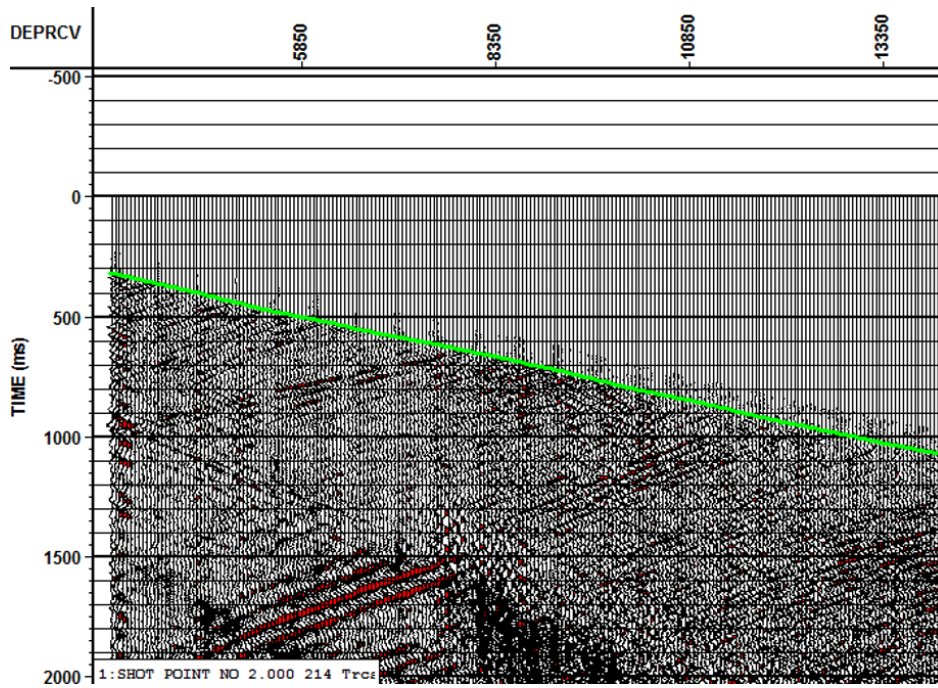


Figure 19 Upgoing P & S wavefields on perpendicular-component (P) of an offset VSP common-shot gather after filtering out downgoing wavefields.

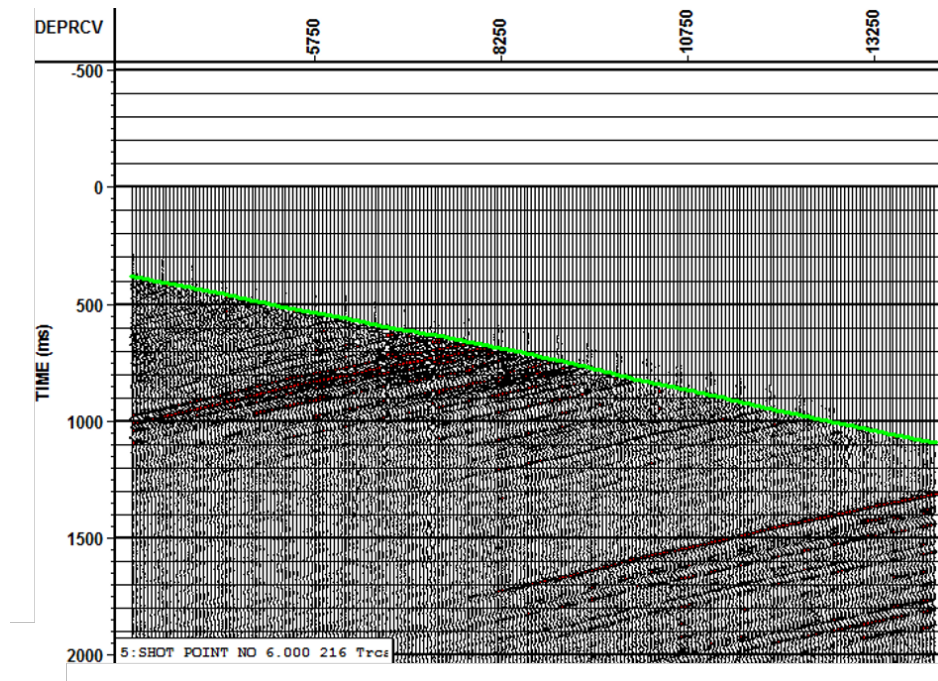


Figure 20 Vertical-component after inverse-vertical rotation

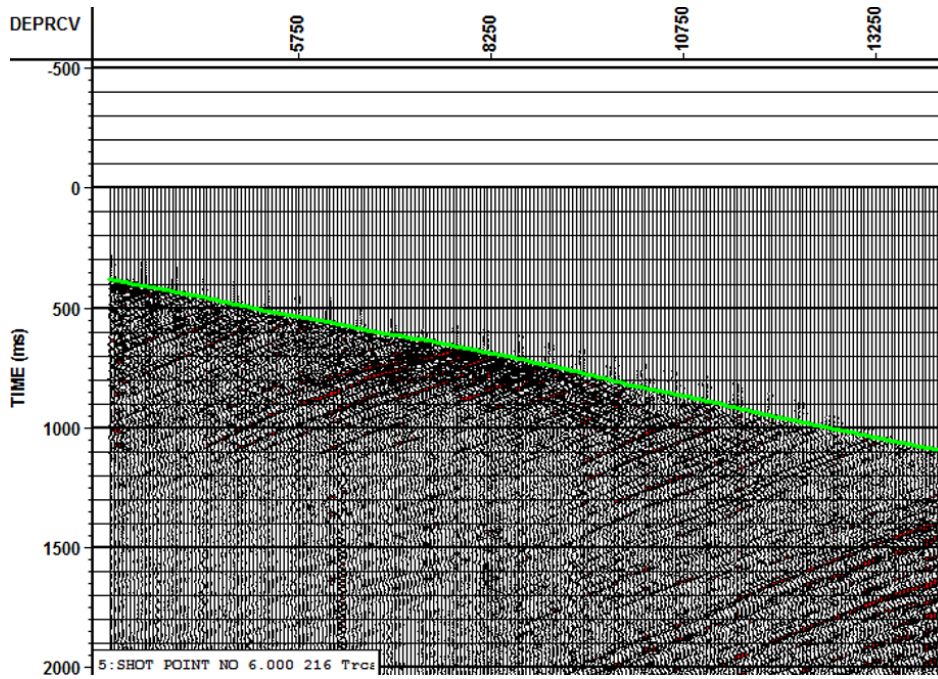


Figure 21 Radial-component after inverse-vertical rotation

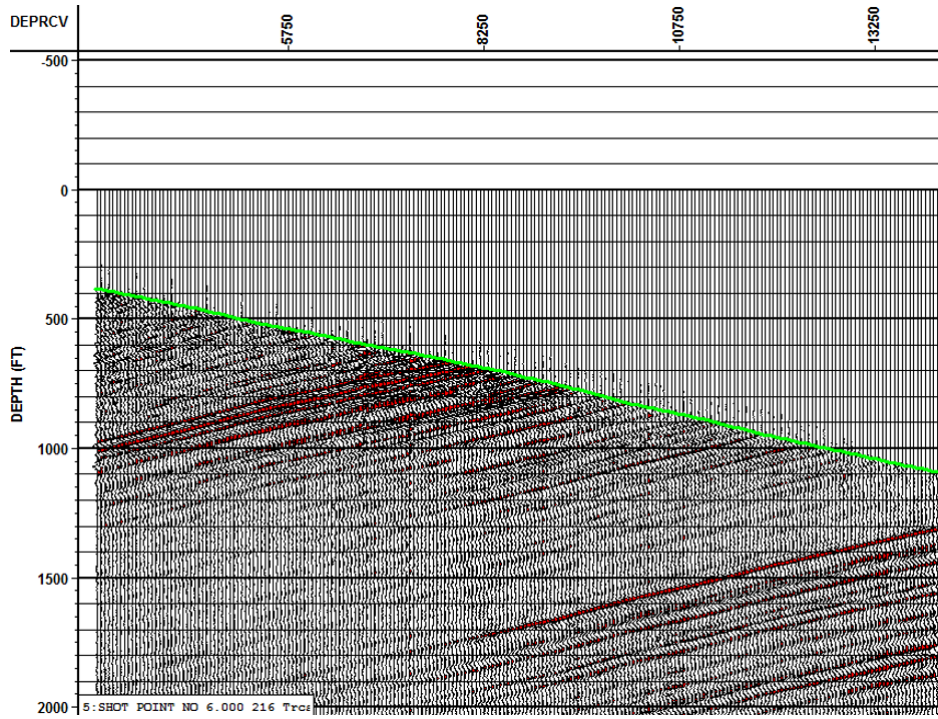


Figure 22 Upgoing P wavefield after model-based rotation.

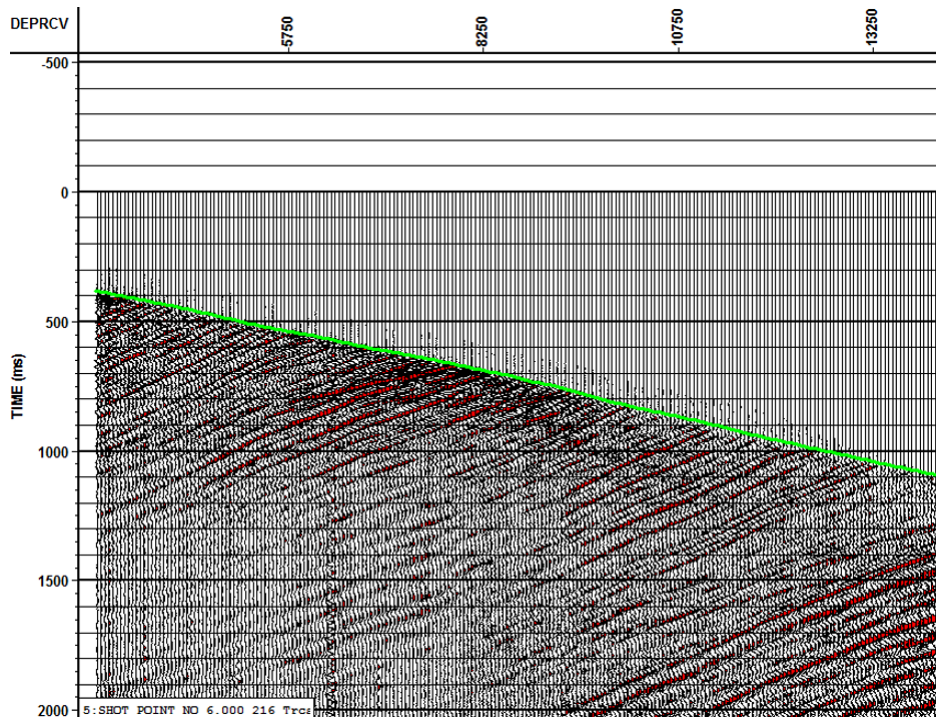


Figure 23 Upgoing S wavefield after model-based rotation.

AVAZ ANALYSIS FOR OFFSET VSPS

For the oil target, Wasatch-180, it took 36 iterations to minimize the difference between the measured data and theoretical reflectivity calculated by Ruger (1996). The values obtained for intercept, isotropic gradient, anisotropic gradient, and isotropy plane orientation were respectively -0.003, .001, 0.027, and -30° clockwise from North. For the gas target, Upper Green River formation, there was much less data available at its depth of 5750,' as can be seen by Figure 2. That can affect the credibility of the results negatively.

From the VSP-CDP transform, the reflectivity vs offset amplitude curves of different VSP shots were extracted and are shown at the top of Figure 25. The angles of incidence were calculated using Snell's law as explained in Chapter 4. The reflectivity vs angle of incidence amplitude curves of different VSP shots are shown at the bottom Figure 25. AVAZ using linearized Ruger's code, explained in Al Dulaijan (2017), is implemented. It took 11 iterations to minimize the objective function. The inverted values for intercept, isotopic gradient, anisotropic gradient, and isotropy plane orientation were respectively -0.0125, 0.0612, 0.0168, and -89° from North.

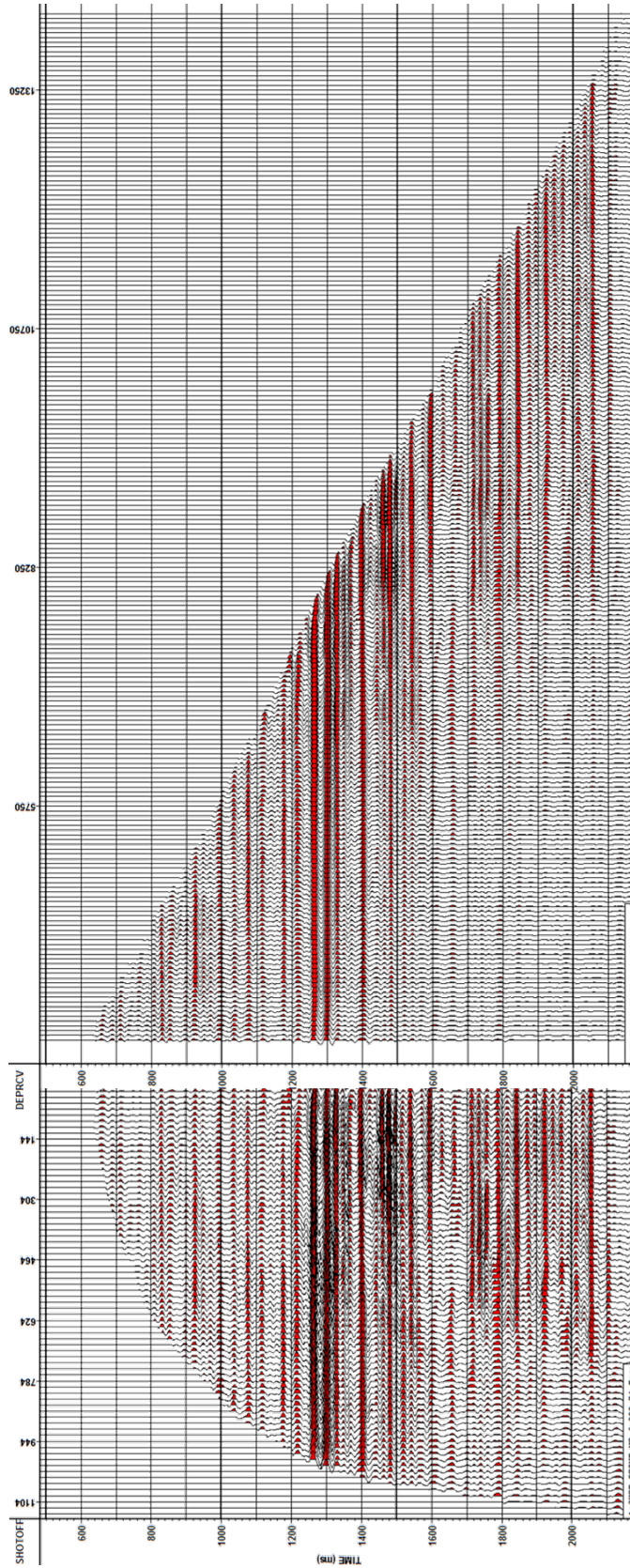


Figure 24 VSP-CDP transform (left) and NMO-corrected upgoing P wave.

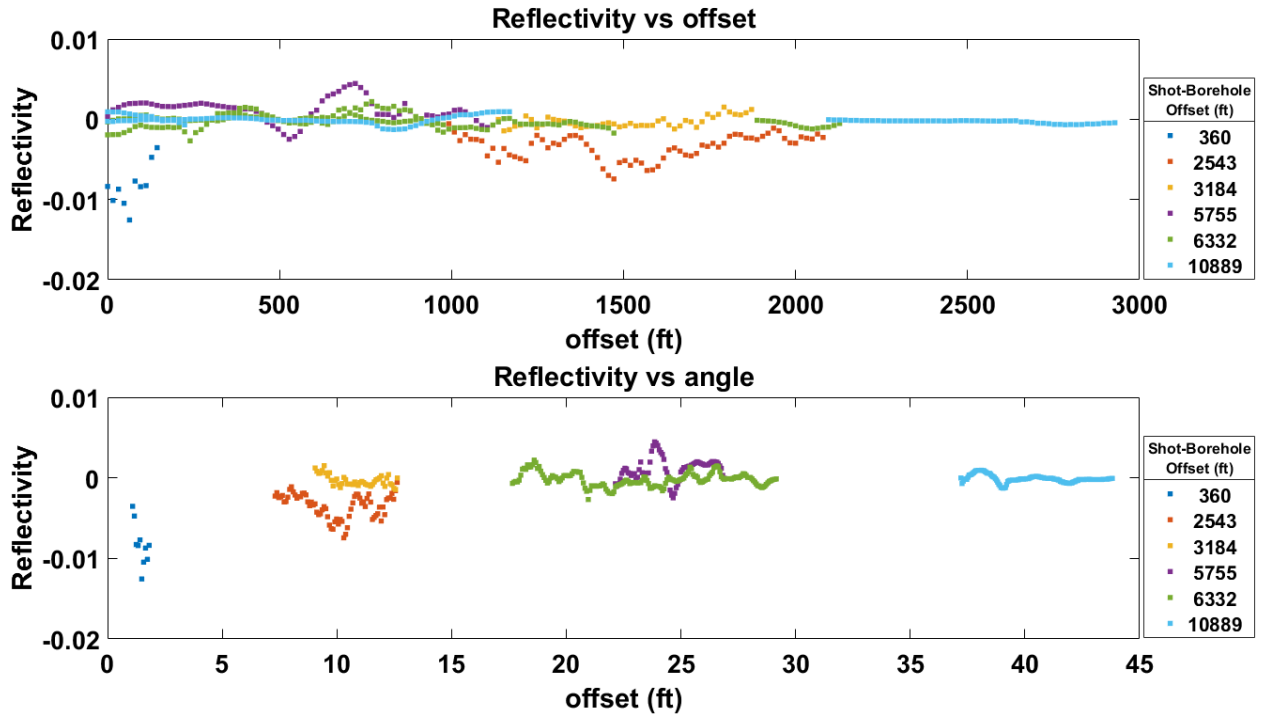


Figure 25 Reflectivity vs offset (top), and reflectivity vs angle of incidence (bottom).

VVAZ ANALYSIS FOR OFFSET VSPS

Prior to VVAZ analysis, first arrival times were manipulated to reflect surface seismic RMS velocities and to account for the varying surface elevation. A schematic diagram showing the borehole and downgoing raypath from shot to geophone, indicated by black arrow are shown in Figure 26Figure 27. X is the borehole-shot offset. Vertical raypath from shot elevation is indicated by a red arrow. The blue arrow indicates the vertical raypath to the Seismic Reference Datum (SRD) . The shot to geophone traveltime is calculated from SDR and indicated by green arrow. And finally, the traveltime from SRD is doubled, so the geophone can be treated as a CDP in surface seismic geometry. The equations were derived using geometry as below:

$$VT_{SE} = TT_{SE} \cdot \cos(\tan^{-1}[\frac{x}{MD-KB+SE}]), \quad (2)$$

$$VT_{SRD} = VT - \frac{SE-B}{V_{avg}} + \frac{SRD-B}{V_r}, \quad (3)$$

and

$$TT_{SRD} = \frac{VT_{SRD}}{\cos(\tan^{-1}[\frac{x}{MD-KB+SE}]}, \quad (4)$$

where TT_{SE} is first arrival times indicated by the black arrow from shot directly to geophone on Figure 3. VT_{SE} is the vertical time from geophone to shot elevation, and is indicated by the red arrow. TT_{SRD} is the first arrival time from geophone to shot to SRD, and it is indicated by the green arrow. MD is the measured depth of geophone from KB . SE is the shot elevation. Finally, B , V_{avg} , and V_r are respectively base of weathering, average velocity, and replacement velocity.

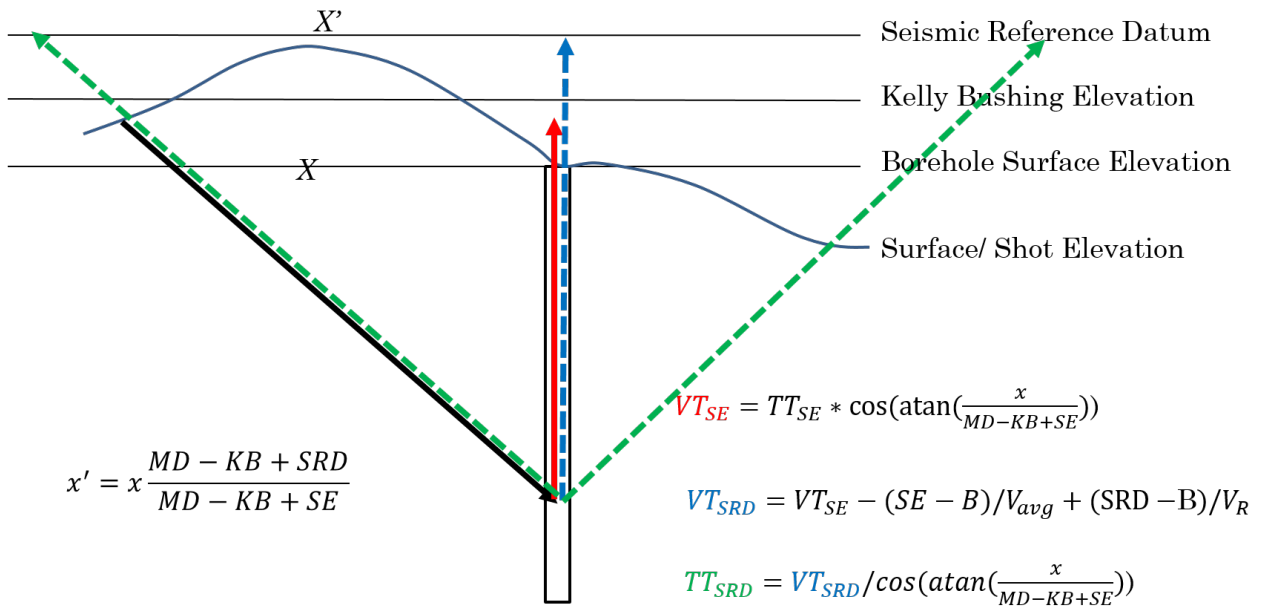


Figure 26 A schematic diagram showing borehole and downgoing raypath from shot to geophone, indicated by black arrow. X is the borehole-shot offset. Vertical raypath from shot elevation is indicated by red arrow. Blue arrow indicates vertical raypath to SRD. The shot to geophone traveltimes is calculated from SDR and indicated by green arrow.

For all VSPs, each receiver represents a CDP of conventional surface seismic survey. The corrected arrival times or the double of TT_{SRD} (Equation 4) for all VSPs are used for the VVAZ inversion. Vertical arrival times were inverted and compared to VT_{SRD} in Equation (3) calculated for all VSPs. Inverted arrival times agreed closely with those of shots 2, 4, and 6 and agreed somewhat less well with those of shot 3, 5, 7 and 8, as can be seen in Figure 27. Calculated vertical arrival times of all shots were not in very close agreement at the beginning. Irregular topography and the near surface were not corrected for precisely enough. That is a shortcoming of using RMS velocities for VVAZ. A better solution would be to use an accurate interval algorithm. Inverted RMS velocities are shown in Figure 28 where the blue curve indicates the fast RMS velocity and the red curve indicates the slow RMS velocity. The orientation of the fast RMS velocity for all depths can be seen in the circular histogram in Figure 29. We have estimated Dix-type interval properties of anisotropy in Figure 30. The intervals used to calculate the ellipse coefficients involved every receiver (or 50'). On the left are the fast (blue) and slow (red) interval

velocities. In the middle is the anisotropy intensity, and on the right is the interval anisotropy direction.

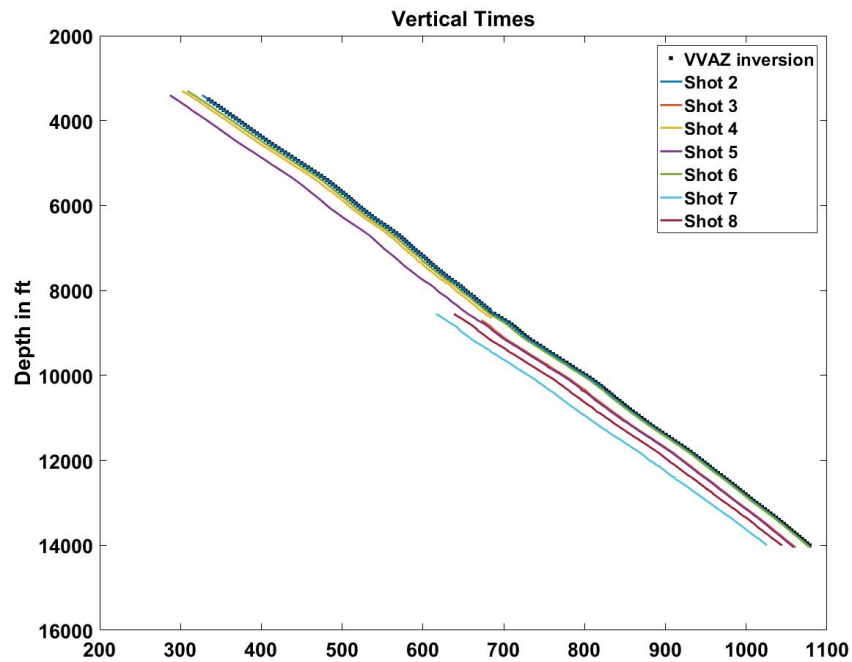


Figure 27 Vertical arrival times in ms of VVAZ inversion vs. calculated vertical traveltimes for each VSP shot.

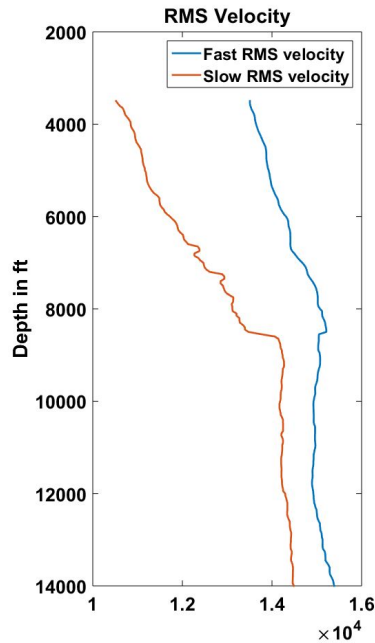


Figure 28 Inverted fast RMS velocity (blue) and slow RMS velocity (red).

Orientation of fast RMS velocity for all levels

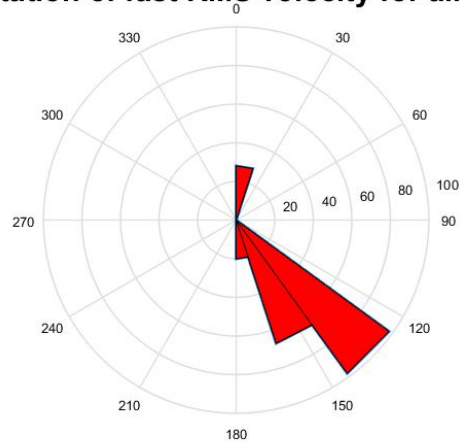


Figure 29 Circular histogram of fast RMS velocity direction for all receivers.

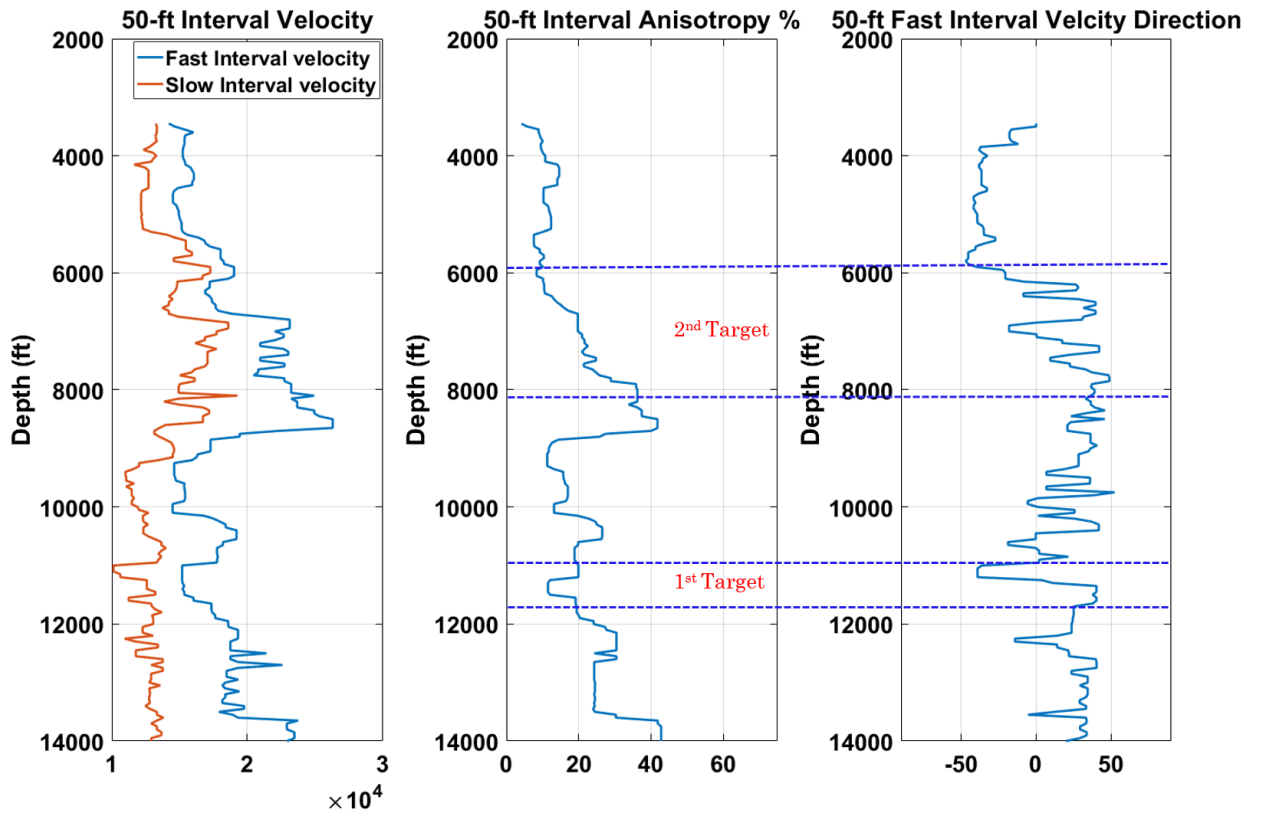


Figure 30 50'-interval anisotropy: slow and fast RMS velocity (left), anisotropy intensity (middle), and anisotropy direction (right).

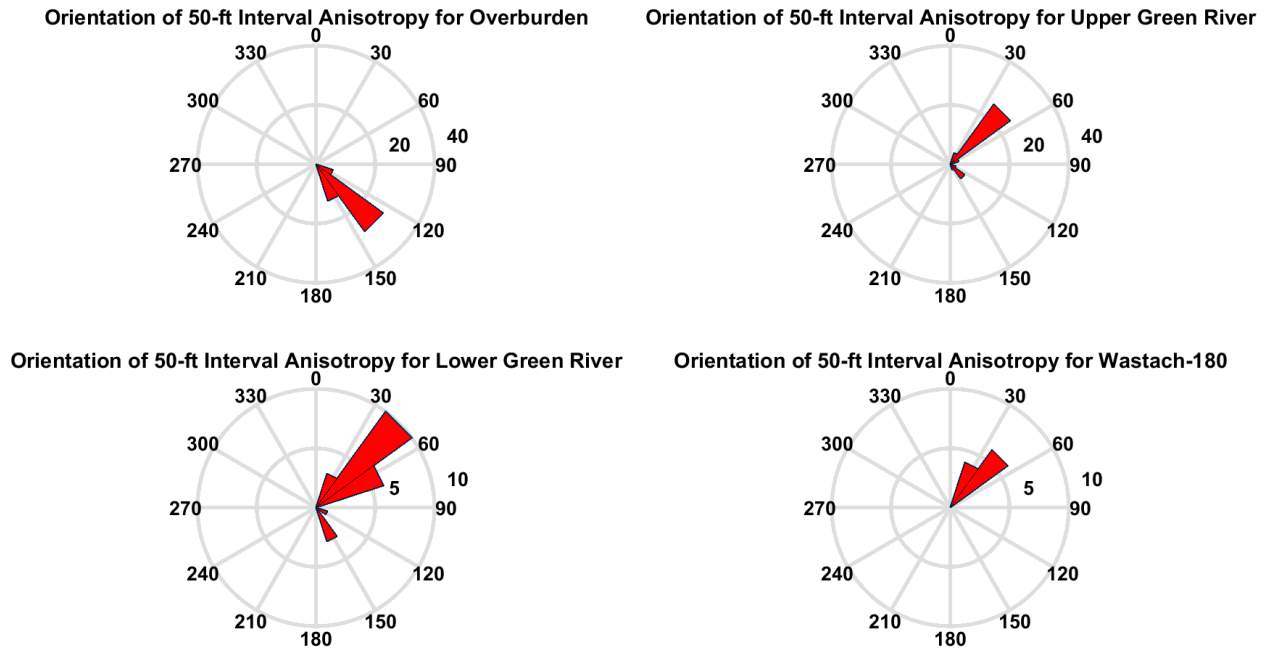


Figure 31 Circular histogram showing the orientation of 50' interval anisotropy of: overburden, Upper Green River, Lower Green River, and Wasatch-180.

S-WAVE SPLITTING FOR 4-C VSP

In HTI media, the P wave is fastest along the fracture planes, slowest perpendicular to fracture planes, and intermediate in other directions. On the other hand, the S wave splits into two phases; a phenomenon known as S-wave splitting, S-wave birefringence, or S-wave double-refraction. Polarizations of the two S waves are determined by the anisotropic axis of symmetry. The fast S is polarized along the fracture planes, and the slow S is perpendicular to the fracture planes. Beside the anisotropic axis of symmetry, the velocity of an S wave is controlled also by the angle of incidence and the azimuth of propagation. The two S waves travel at different velocities and hence are recorded at different times. The delay in time is proportionally related to the degree of S-wave anisotropy and the thickness of the anisotropic medium (Crampin, 1981).

The method is tested on a physical modeling dataset. It is applied to the common-receiver gathers from the second dataset illustrated in Al Dulaijan (2017). For all common-receiver gathers, horizontal components of receivers and sources were aligned along either the x- or y-axis. In other words, they were aligned either parallel to the fracture plane or normal to the fracture plane. With this orientation, an S wave is fast along y-axis and slow along x-axis. In other directions, the S wave undergoes S-wave splitting and repolarizes along fast and slow directions. The fast S wave should mostly be recorded by V_{11} and the slow S wave by V_{22} . Energy on V_{12} and V_{21} should be minimal. This was not the case in our experiment! That suggests an error in the polarization direction of the horizontal transducers.

An Alford 4-component rotation (Alford, 1986) can be used to statistically rotate horizontal components (V) recorded in acquisition recorded system into anisotropy natural coordinate system (U) using rotation matrix ($R(\theta)$):

$$V = \begin{bmatrix} v_{11} & v_{12} \\ v_{21} & v_{22} \end{bmatrix}, \quad (6)$$

$$U = \begin{bmatrix} u_{11} & u_{12} \\ u_{21} & u_{22} \end{bmatrix}, \quad (7)$$

and

$$R(\theta) = \begin{bmatrix} \cos \theta & \sin \theta \\ -\sin \theta & \cos \theta \end{bmatrix} \quad (8)$$

The rotation matrix, $R(\theta)$ is an orthogonal matrix that gives the identity matrix when multiplied by its transpose or its inverse. To find a new basis for the natural coordinate system, the counterclockwise rotation by angle (θ) is

$$U = R(\theta) V R^T(\theta). \quad (9)$$

Substituting equations (6), (7), and (8) into equation (9):

$$\begin{bmatrix} u_{11} & u_{12} \\ u_{21} & u_{22} \end{bmatrix} = \begin{bmatrix} \cos^2 \theta v_{11} + \sin^2 \theta v_{22} + 0.5 \sin 2\theta (v_{21} + v_{12}) & \dots \\ \cos^2 \theta v_{21} - \sin^2 \theta v_{12} + 0.5 \sin 2\theta (v_{22} - v_{11}) & \dots \\ \dots & \cos^2 \theta v_{12} - \sin^2 \theta v_{21} + 0.5 \sin 2\theta (v_{22} - v_{11}) \\ \dots & \cos^2 \theta v_{22} + \sin^2 \theta v_{11} - 0.5 \sin 2\theta (v_{21} - v_{12}) \end{bmatrix}. \quad (10)$$

Equation (10) transforms V , horizontal components in acquisition coordinate system into the natural coordinate system (Alford, 1986).

The rotation angle (θ) is found by scanning different angle values, and selecting the angle that minimizes u_{12} and/or u_{21} . For each common-receive gather, angles were scanned within a time window to determine the rotation angle (θ) and Alford rotation was applied. Please refer to the 2nd dataset in Al Dulaijan (2017). The two linear gathers with 0° and 90° azimuths respectively are shown by Figure 32 and Figure 33 before rotation in the left and after the rotation on the right. Alford rotation was applied to the second dataset. Figures 16, 18, and 20 show the unrotated data and the rotated data of the second dataset that was acquired over the Phenolic medium. The cross energy of the 90°-azimuth shot gather common-shot gather, is shown in **Error! Reference source not found.**

Alford rotation behavior is just as anticipated. The rotation angles are very small because acquisition coordinate system is similar to the natural coordinate system. The small

angles are caused by small errors in acquisition. The results of Alford rotation for the second dataset are quite satisfying. They provide confidence in S-wave acquisition tools.

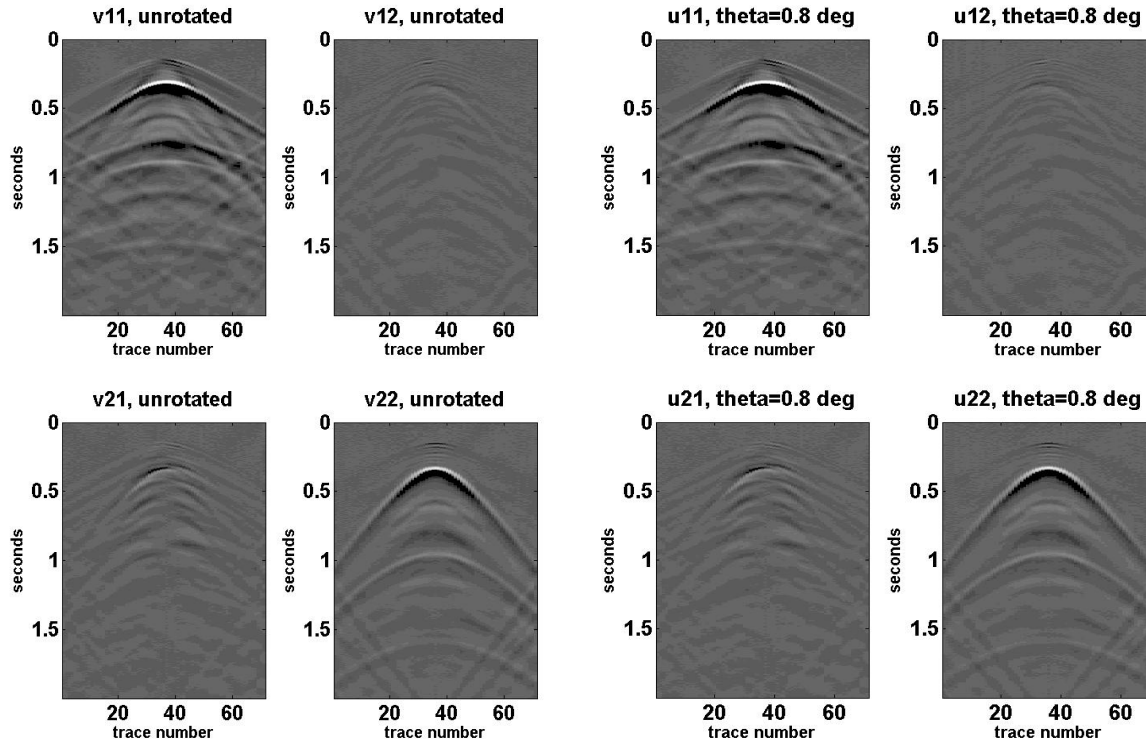


Figure 32 0°-azimuth shot gather acquired over the phenolic layer: 4 Horizontal components before rotation (left) and after rotation (right).

The 4 components of the 4-C VSP, in Altamont-Bluebell data are shown in Figure 35. Prior to applying 4-C rotation to the 4-components, the two horizontal components of the geophones are needed to be re-oriented into East-West and North-South directions. Luckily other VSP shots were acquired with the recording tool in place. Those shots were used to re-orient the tool by first using the P-wave first breaks from other shots to calculate the required angle to re-orient to that shot. And later, re-orient the tool into East-West and North-South directions. For Alford rotation, angles were scanned within a picked time window placed approximately centered on first S-wave arrival times to determine the rotation angle (θ). For layer stripping, all data below the depth at which S-wave polarization change is observed are rotated. Then, a static time shift is applied to remove the lag between fast and slow S waves at that depth. This technique simulates placing a source at the depth where S-wave polarization changes (Winterstien and Meadows, 1991). This layer-stripping method was applied to the 4 layers: overburden, Upper Green River formation, Lower Green River formation, and Wasatch formation. For the last layer, which is the Wasatch-180 formation, Alford rotation was also applied. The four components of VSP data after rotation and layer stripping and the required rotation angle are shown in Figure 36 and Figure 37 respectively. Figure 38 shows an overlay of fast S-wave in blue traces and slow

S-wave in red traces, while Figure 39 shows Fast S-wave first arrival times indicated by blue, and slow S-wave indicated by red.

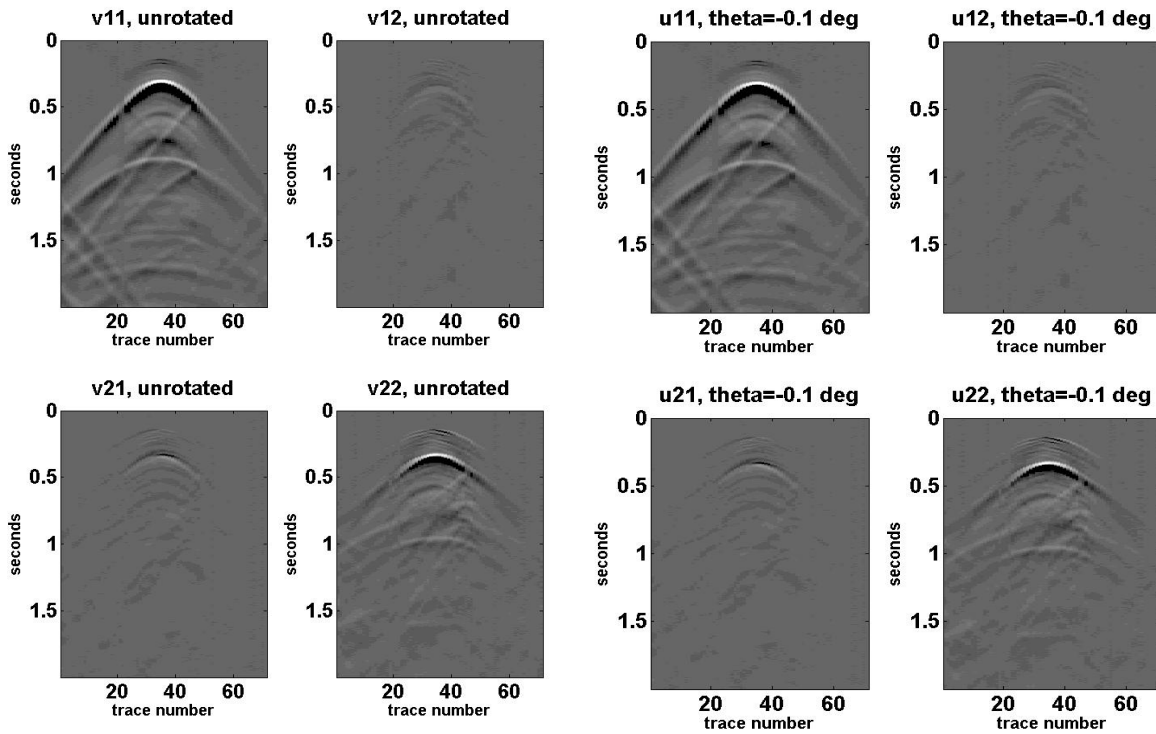


Figure 33 90°-azimuth shot gather acquired over the phenolic layer: 4 Horizontal components before rotation (left) and after rotation (right).

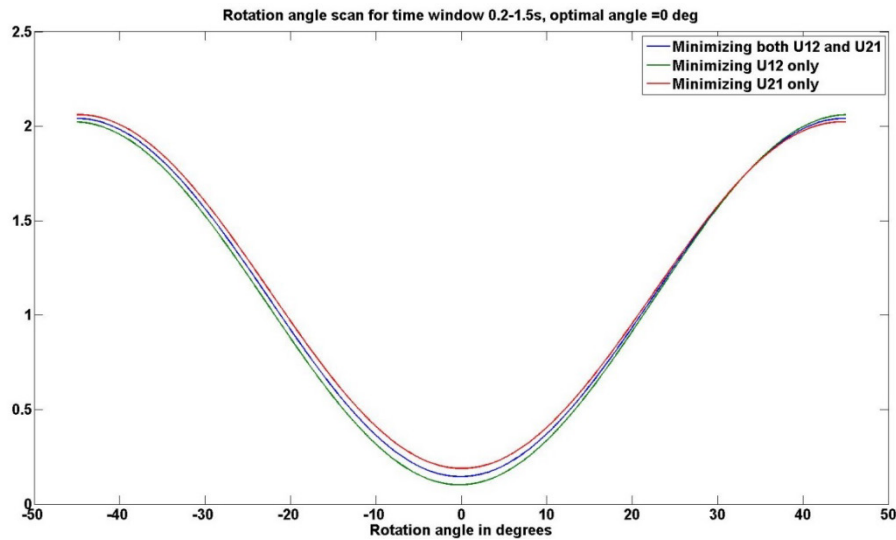


Figure 34. 90°-azimuth shot gather: cross energy vs. rotation angle.

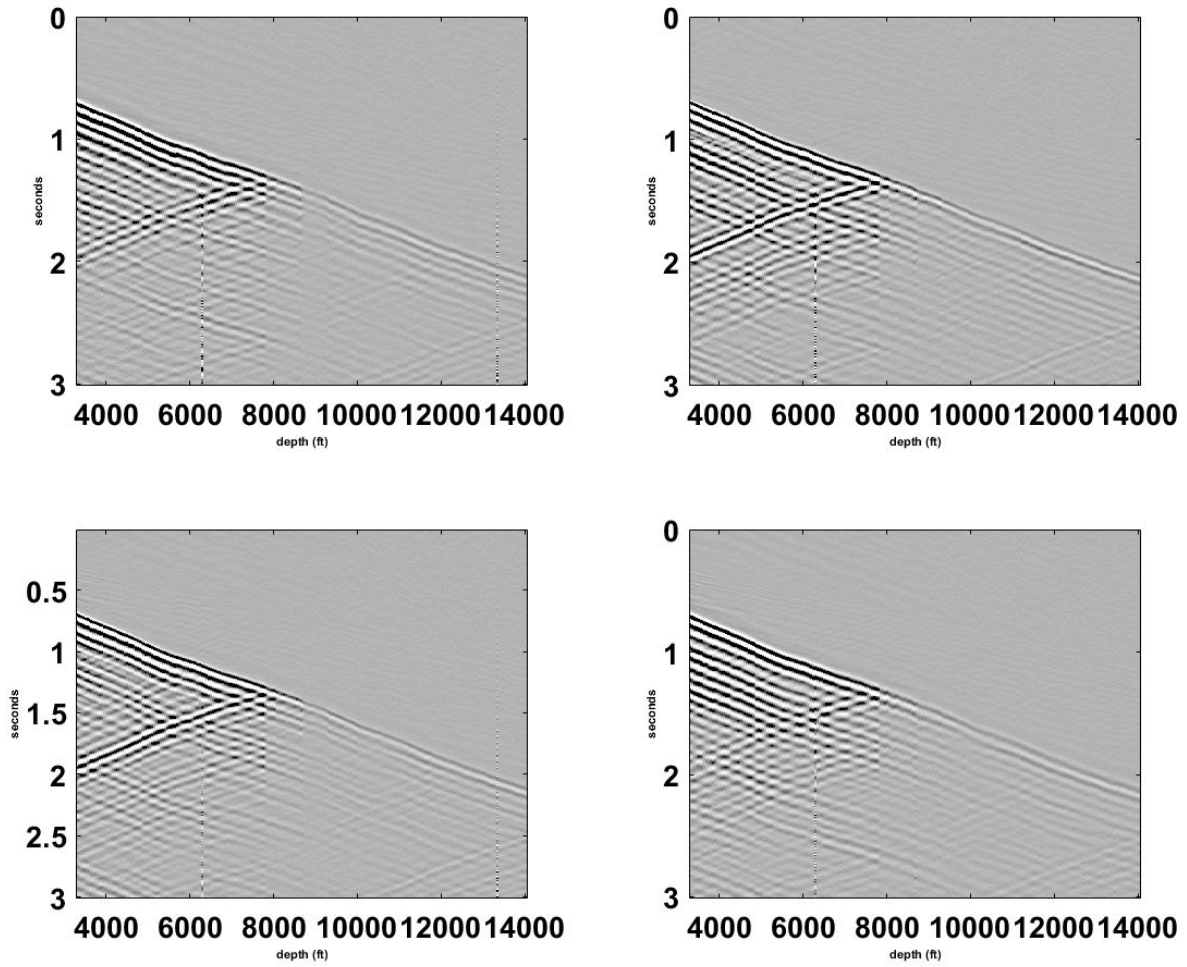


Figure 35 4-C VSP before rotation: N-S shot components (top), E-W shot components (bottom), N-S receiver components (left), and E-W receiver components (right).

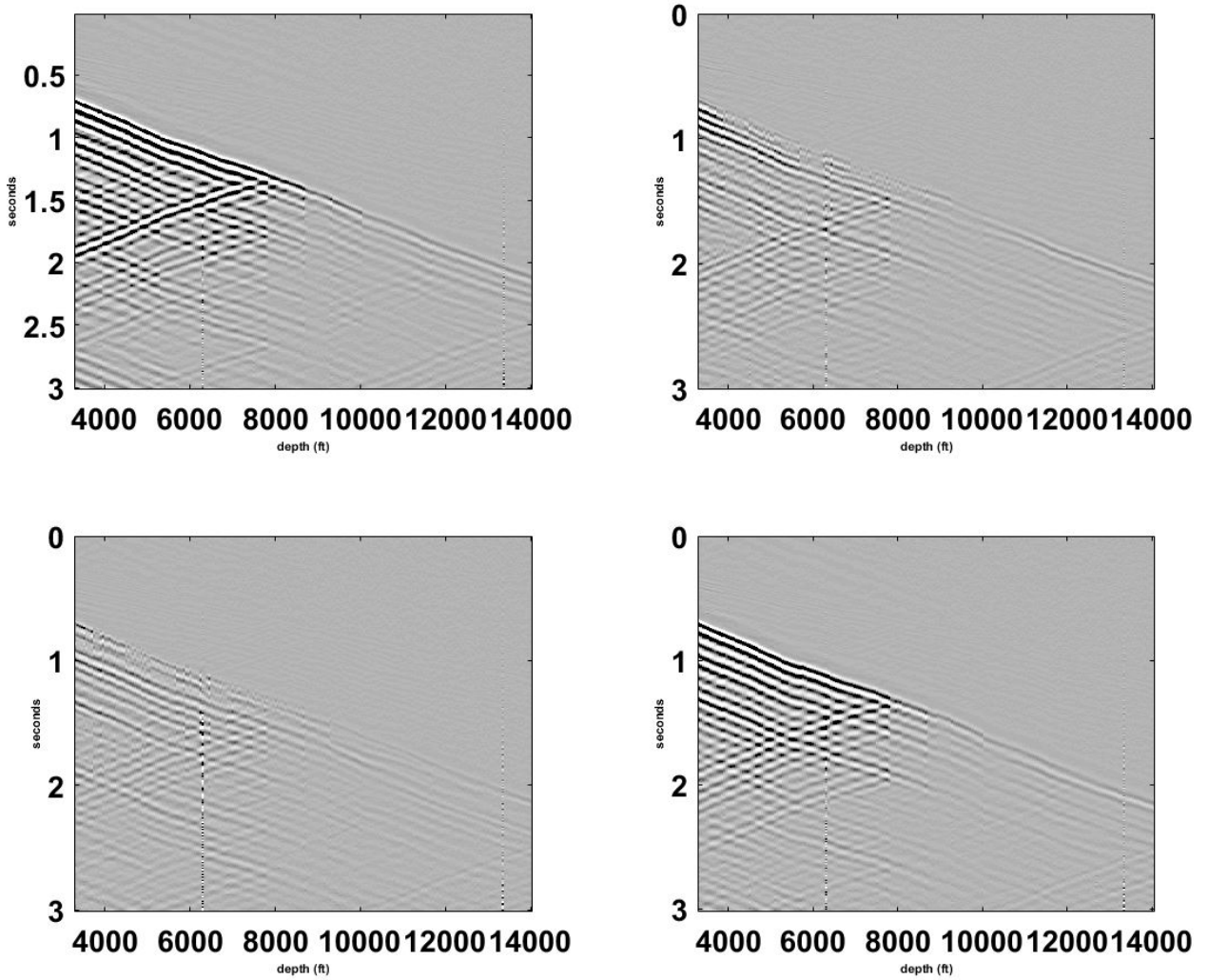


Figure 36 VSP after rotation and layer stripping: N-S shot components (top), E-W shot components (bottom), N-S receiver components (left), and E-W receiver components (bottom).

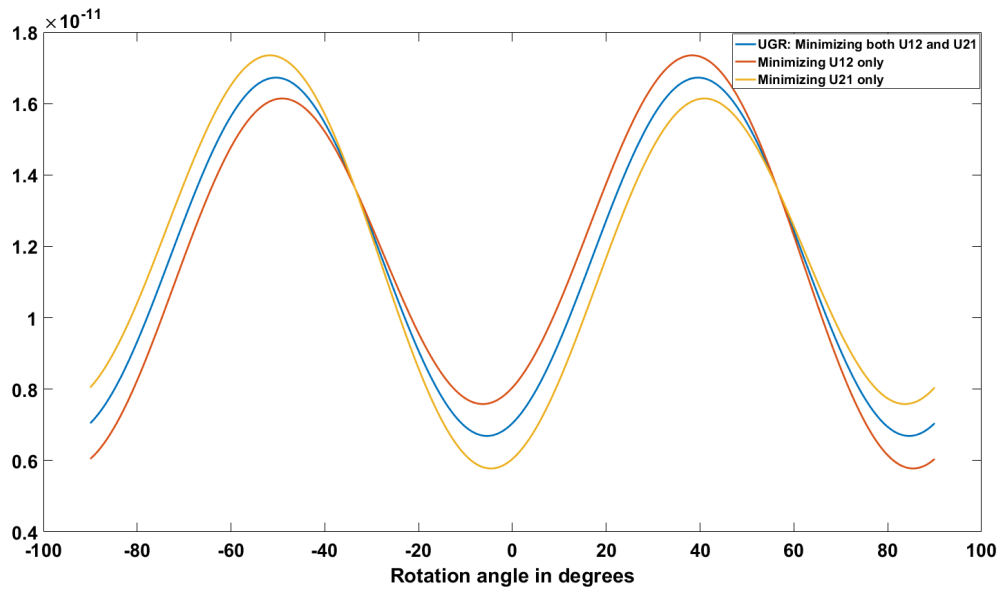


Figure 37 4-C VSP cross energy vs. rotation angle of: overburden, Upper Green River.

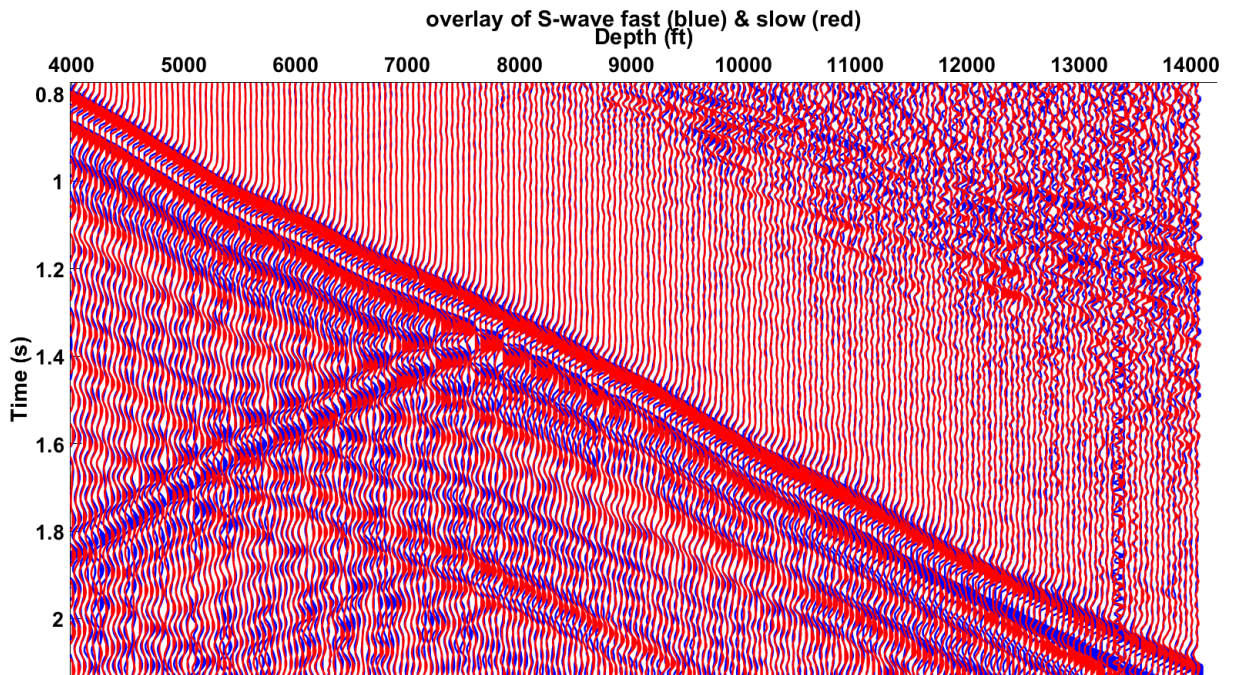


Figure 38 S-wave data after rotation and layer stripping of 4-C VSP. The S-wave fast is indicated by blue traces, while slow is indicated by red traces.

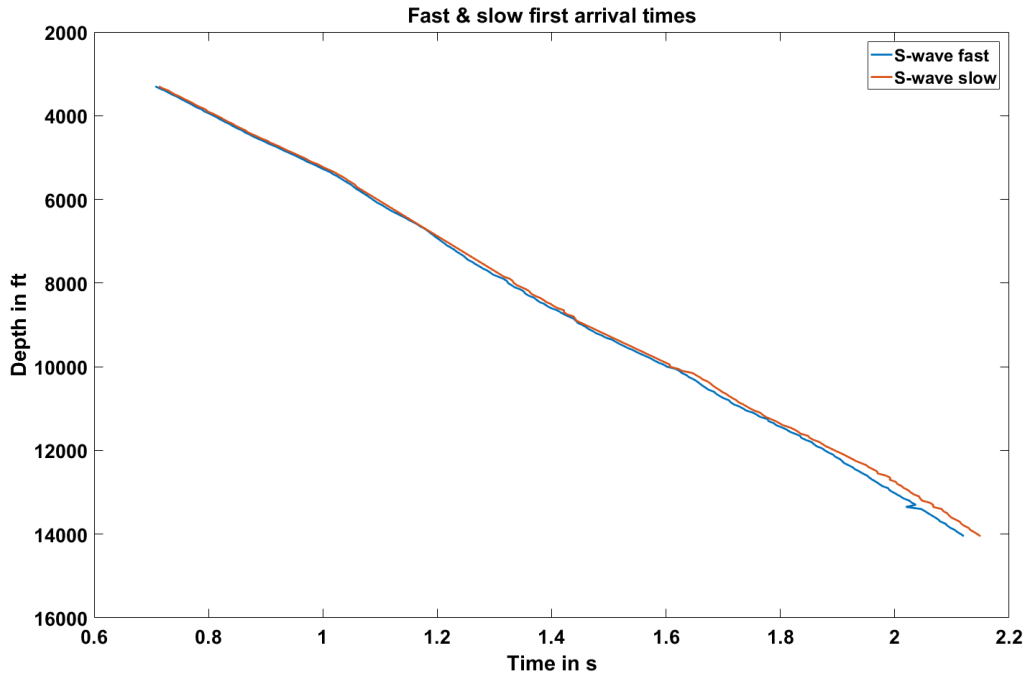


Figure 39 Fast S-wave first arrival times indicated by blue, and slow S-wave indicated by red.

The plot of cross energy against rotation angle is shown in Figure 40 for the 4 layers analyzed. The rotation angles of overburden, Upper Green River formation, Lower Green River formation, and Wasatch-180 formation were found to be as follows: The Upper and Lower green river formation have anisotropy orientation of NW-SE, while the overburden and Wasatch formation have anisotropy orientation of NE-SW. The fast S-wave and slow S-waves were picked on rotated data. The picks are shown in Figure 39 with blue picks being fast S-wave and red picks being slow S-waves. From the lag between the two modes of S-wave, an anisotropy intensity log is calculated in the left side of Figure 40, while the anisotropy direction is shown on the right in the same figure. At the borehole location, the Wasatch formation has the most anisotropy intensity as can be seen by the anisotropy intensity log just below 10000 feet of depth. Wasatch-180, the oil target, which is within the Wasatch, has less anisotropy than the rest of the Wasatch but more than other formations.

SUMMARY & CONCLUSIONS

For the development of unconventional reservoirs, azimuthal variations of P-wave velocities can be a valuable tool for fracture information. In this paper, we have developed a VVAZ workflow for offset, workaround, or walkaway VSPs using a method for surface seismic. Vertical arrival times for all shots were not very similar at the beginning. Irregular topography and near surface effects were not corrected properly, which would affect the VVAZ method shown here, based on RMS velocity. Therefore, interval anisotropy properties were calculated, as well, to avoid the effects of overburden. The intervals used to calculate the ellipse coefficients involved every receiver (or 50').

The three reservoirs were found to have anisotropy oriented along a NE-SW trend, while the overburden anisotropy was oriented NW-SE. The anisotropy intensity was found to be highest in the Wasatch formation and the lower part of the Upper Green River formation.

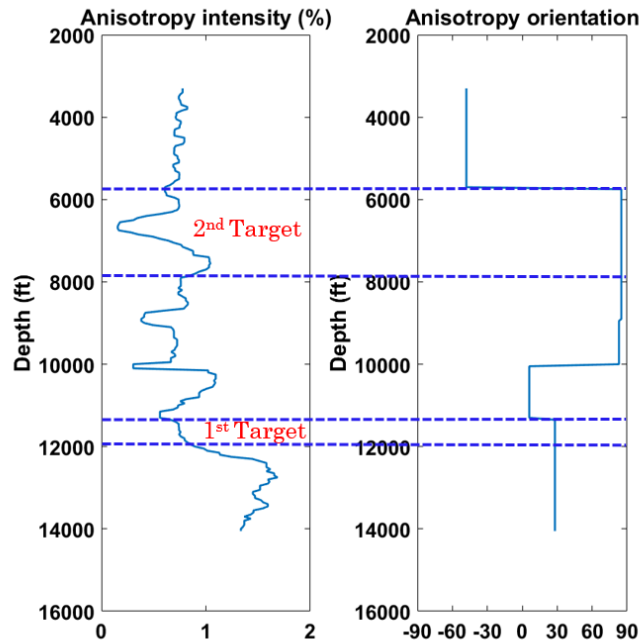


Figure 40 S-wave analysis: anisotropy intensity (left) and direction (right).

ACKNOWLEDGEMENTS

We thank the sponsors of CREWES for their support. We also gratefully acknowledge support from NSERC (Natural Science and Engineering Research Council of Canada) through the grant CRDPJ 379744-08. Also, we are grateful to Devon Energy for permission to use the data and publish the results. We thank Schlumberger for the use of VISTA® software. The first author would like to thank Dr. Jon Downton, and Khalid Alumteri for useful discussions. He thanks David Henley for proofreading this report. Also, he would like to thank Saudi Aramco for graduate study sponsorship.

REFERENCES

- Al Dulaijan, K., 2017, Inversion of azimuthal velocity and amplitude variations for seismic anisotropy. Ph.D. thesis: University of Calgary.
- Alford, R. M., 1986, Shear data in the presence of azimuthal anisotropy: Dilley Texas, SEG Expanded Abstracts, SEG Annual Convention.
- Crampin, S., 1981, A review of wave motion in anisotropic and cracked elastic-media. *Wave motion*, 3(4), 343-391.
- Rüger, A. 1996. Reflection coefficients and azimuthal AVO analysis in anisotropic media. Ph.D. thesis, Colorado School of Mines, Dept. of Geophysics, Golden, Colorado, USA.
- Winterstein, D. F., & Meadows, M. A., 1991, Shear-wave polarizations and subsurface stress directions at Lost Hills field. *Geophysics*, 56(9), 1331-1348.